Modeling Low-Pressure Nanofiltration Membranes and Hollow Fiber Modules for Softening and Pretreatment in Seawater Reverse Osmosis

by

Omar Labban

B.S.M.E., American University in Dubai (2014)

Submitted to the Department of Mechanical Engineering
in partial fulfillment of the requirements for the degree of

Master of Science in Mechanical Engineering

at the

MASSACHUSETTS INSTITUTE OF TECHNOLOGY

June 2016

Author ..... Signature redacted .....
Department of Mechanical Engineering
May 20, 2016

Certified by ..... Signature redacted .....
John H. Lienhard V
Abdul Latif Jameel Professor of Water
Thesis Supervisor

Accepted by ..... Signature redacted .....
Rohan Abeyaratne
Chairman, Committee on Graduate Students

Modeling Low-Pressure Nanofiltration Membranes and Hollow Fiber Modules for Softening and Pretreatment in Seawater Reverse Osmosis

by

Omar Labban

Submitted to the Department of Mechanical Engineering
on May 20, 2016, in partial fulfillment of the
requirements for the degree of
Master of Science in Mechanical Engineering

Abstract

Recently, interest in nanofiltration (NF) has been surging, as has interest using it as a technology for better brine management and pretreatment in reverse osmosis (RO) plants. Using NF for pretreatment reduces fouling and scaling in RO units, allowing for potentially higher recoveries. This lowers the environmental impact of RO by decreasing the amount of water to be treated per unit volume of water produced, and reducing the volume of RO brine to be managed. This can potentially curb the CO_2 emissions resulting from the RO desalination process.

A novel class of low-pressure nanofiltration (NF) hollow fiber membranes, particularly suited for water softening and desalination pretreatment have lately been fabricated in-house using layer-by-layer (LbL) deposition with chemical crosslinking. These membranes can operate at exceedingly low pressures (2 bar), while maintaining relatively high rejections of multivalent ions. In spite of their great potential, our understanding as to what makes them superior has been limited, demanding further investigation before any large-scale implementation can be realized.

In this study, the Donnan-Steric Pore Model with dielectric exclusion (DSPM-DE) is applied for the first time to these membranes to describe the membrane separation performance, and to explain the observed rejection trends, including negative rejection, and their underlying multi-ionic interactions. Experiments were conducted on a spectrum of feed chemistries, ranging from uncharged solutes to single salts, salt mixtures, and artificial seawater to characterize the membrane and accurately predict its performance.

Modeling results were validated with experiments, and then used to elucidate the working principles that underly the low-pressure softening process. An approach based on sensitivity analysis shows that the membrane pore dielectric constant, followed by the pore size, are primarily responsible for the high selectivity of the NF membranes to multivalent ions. Surprisingly, the softening process is found not to be sensitive to changes in membrane charge density. Our findings demonstrate that

the unique ability of these membranes to exclusively separate multivalent ions from the solution, while allowing monovalent ions to permeate, is key to making this low-pressure softening process realizable.

Given its high surface area to volume ratio and desirable mass transfer characteristics, the hollow fiber module configuration has been central to the development of reverse osmosis (RO) and ultrafiltration (UF) technologies over the past five decades. Following the development of the LbL membrane, interest in their scale-up implementation for softening and desalination pretreatmenthas been growing. Further progress on large-scale deployment, however, has been restrained by the lack of an accurate predictive model, which is pivotal to guiding module design and operation.

Earlier models targeting hollow fiber modules are only suitable for RO or UF technologies, and no appropriate NF models have been presented to characterize the performance of hollow fiber modules at the large-scale. In this work, we propose a new modeling approach based on the implementation of mass and momentum balances, coupled with a suitable membrane transport model, such as the Donnan-Steric Pore Model with dielectric exclusion (DSPM-DE), to predict module performance at the system-level. We then propose a preliminary module design, and employ parametric studies to investigate the effect of varying key system parameters and to elucidate the tradeoffs available to the module designer.

The model has significant implications for low-pressure nanofiltration, as well as hollow fiber NF module design and operation. An approach based on comparing the marginal increase in system recovery to the marginal increase in transmembrane pressure (TMP) was used to define an optimal operating point. Our findings reveal that increasing the TMP could potentially increase energy savings under some operating conditions.

Thesis Supervisor: John H. Lienhard V
Title: Abdul Latif Jameel Professor of Water

Acknowledgments

First and foremost, I would like to extend my utmost gratitude to my advisor and mentor, Professor John H. Lienhard V, without whom this work might not have been possible. Professor Lienhard, I wish to express my sincere thanks for seeing in me the successful engineer I have always aspired to be, for believing in my talent all along, for trusting and supporting me even during the darkest of times, and for never sparing any effort to point me in the right direction. For your endless trust and support, I shall always be grateful.

To my labmates, I wish to thank everyone of you for your invaluable feedback during group meetings and discussions. Your advice has always been helpful to the work since its infancy, and has inspired several aspects of it as you can tell. To Ronan, Greg, Emily, Leo, Jai, Karim, Kishor, and Hyung, I wish to thank you earnestly for being my second family away from home, and for constantly having my back. To Urmi, I wish to thank you for introducing me to the fascinating world of nanofiltration, and for all your input and advice. Thank you all for making the lab the great work environment it is.

MIT, thank you for giving me the two most beautiful, yet most challenging, years of my life. Thank you for setting the bar up high, for pushing me to the very limit, and for dismantling and rebuilding me to the person I am today. I shall always remain grateful for giving me the opportunity to work alongside the best, and to learn from the brightest. To all MIT professors I have come across, or interacted with, thank you for teaching me how to think, and to look at things differently. Nothing will look the same from now on.

To everyone who has taught me something, challenged me, or sparked my intellect at some point, I wish to thank you for making a difference in my life. To my fellow professors and teachers back home I say thank you for instilling in me the discipline, drive, and above all, passion for what I do. Professors Kwon, Abraham, and Peiman, thank you for supporting me since the very beginnings, and for introducing me to the art and science of engineering. Professor Kwon, thank you for teaching me how to

dream and achieve, and for instilling in me the passion for mechanical engineering.

Of course, my success would never be complete without my family, the reason for my very existence, and whose presence has always added meaning and color to my life. To my mom, dad, and siblings I say thank you for showing me the true meaning of unconditional love. With all the commitments I had to undertake to reach this point, I wish to sincerely say thank you for your patience throughout the years, and hope you forgive me for being away. For all the hardships you had to endure and challenges you had to overcome, it is really your efforts that are paying off today. To my friends at MIT, AUD, and beyond, thank you for standing by my side, and for being constant sources of inspiration and support.

I wish to acknowledge Mrs. Leslie Regan for her support and care that knows no bounds, and Ms. Christine Gervais for her continuous help and thoughtfulness. I acknowledge the phenomenal Dr. Liu Chang and Prof. Chong Tzyy Haur of the Singapore Membrane Technology Centre (SMTC) at the Nanyang Technological University (NTU) for a wonderful research collaboration. I wish to end my acknowledgments by expressing my gratitude to Mr. A. Neil Pappalardo for his generosity in offering me a Pappalardo fellowship to attend MIT, and to the Singapore-MIT Alliance for Research and Technology (SMART) Centre for funding this work.

Omar Labban

Contents

List of Figures

List of Tables

THIS PAGE INTENTIONALLY LEFT BLANK

Nomenclature

Roman Symbols

a_S	Solvent activity
a_i	Solute activity, mol/m^3
A	Debye–Hückel constant, m$^{3/2}$/mol$^{1/2}$
A_c	Flow cross-sectional area, m^2
A_k	Membrane porosity
c_i	Solute concentration, mol/m^3
d_i	Fiber inside diameter, m
d_o	Fiber outside diameter, m
CP_i	Concentration polarization factor
$D_{i,module}$	Module inside diameter, m
$D_{i,p}$	Diffusion coefficient in the pore, m^2/s
$D_{i,\infty}$	Diffusion coefficient in the bulk, m^2/s
D_f	Fractal dimension
D_h	Hydraulic diameter, m
$D_{o,module}$	Module outside diameter, m
e	Specific energy consumption, kWh/m^3
e_0	Elementary charge, 1.602×10^{-19} C
f_D	Darcy friction factor
F	Farady constant, 96487 C/mol
I	Ionic strength, mol/m^3
J_v	Permeate flux, m^3/m^2· s

J_i	Solute flux, mol/m^2· s
k	Boltzmann constant, 1.38066×10^{-23} J/K
$k_{c,i}$	Solute mass transfer coefficient, m/s
$K_{i,c}$	Convection hindrance factor
$K_{i,d}$	Diffusion hindrance factor
ℓ	Position in the axial direction, m
L	Module length, m
N_A	Avogadro's number, 6.023×10^{23} mol^{-1}
N_f	Number of fibers in the module
$\dot{N}_i$	Molar flow rate of species i, mol/s
Pe	Péclet number
P_w	Wetted perimeter, m
Q	Volumetric flow rate, m^3/s
r_p	Effective pore radius, m
r_i	Solute Stokes radius, m
R	Universal gas constant, 8.314 J/mol K
R_i	Solute rejection
RR	Recovery ratio
Re	Reynolds number
Sc	Schmidt number
Sh	Sherwood number
T	Temperature, K
V	Channel bulk velocity, m/s
V_S	Solvent molar volume, m^3/mol
x	Position across membrane active layer, m
X_d	Membrane charge density, mol/m^3
z_i	Ion valency

Greek Symbols

δ	Thickness of concentration polarization layer, m
$\Delta\ell$	Cell thickness, m
ΔP	Transmembrane pressure (TMP) across the membrane, Pa
$\Delta\Pi$	Osmotic pressure difference across the membrane, Pa
ΔW_i	Born solvation energy barrier, J
Δx	Thickness of membrane active layer, m
γ_i	Activity coefficient
λ_i	Ratio of solute Stokes radius to effective pore radius
μ	Solvent viscosity, Pa $\cdot$ s
μ_i	Solute electrochemical potential, J/mol
ϕ	Packing density
ϕ_i	Ratio of permeate flux to the uncorrected mass transfer coefficient
Φ_i	Steric partitioning coefficient
Φ_B	Born solvation coefficient
ψ	Electric potential, V
Ψ_f	Correction factor for fractal dimension
ρ	Solution density, kg/m^3
ε	Computed error
ε_0	Permittivity of vacuum, 8.854×10^{-12} F/m
ε_b	Relative permittivity/dielectric constant of the bulk
ε_p	Relative permittivity/dielectric constant of the pore
ε_r	Relative permittivity/dielectric constant
ξ	Electric potential gradient at the feed/membrane interface, V/m
Ξ_i	Mass transfer coefficient correction factor

Subscripts

b	bulk feed solution

D	Donnan
D_h	hydraulic diameter
f	feed
i	Solute identity
in	inlet
L	hydraulic loss
lim	Limiting rejection
m	Membrane/feed interface just outside the pores
p	permeate
set	error predefined threshold
w	condition at the wall

Superscripts

$\bullet$	Mass transfer correction for the suction effect

Chapter 1

Background and Motivation

1.1 Nanofiltration in Water Softening and Desalination Pretreatment

Nanofiltration (NF), introduced in late 1980's, is a membrane process whose performance falls between ultrafiltration (UF) and reverse osmosis (RO); and as its name implies, NF membranes have pore sizes on the order of 1 nm (corresponding to a molecular weight cut-off (MWCO) of 300 – 500 Da) [1]. With their unique selectivities and high permeabilities relative to RO, NF membranes presented a major milestone in membrane technology, have attracted considerable attention since their introduction, and have found numerous applications, spanning numerous fields from water and waste water treatment to biotechnological, pharmaceutical, and food industry applications [2]. A recent review by Mohammad et al. [2] identifies NF as a research domain of surging interest, predicts NF will continue to play a prominent role in membrane technology, and reveals the future prospects and areas of potential growth NF is likely to experience in the long term.

Given its high selectivity for multivalent ions, areas in which NF is projected to grow include softening of hard water feeds, and more recently, desalination pretreatment. While traditional softening technologies, such as lime softening and pellet softening, have been challenged by their large sludge production and chemical con-

sumption, NF has emerged as a viable alternative in the field [3, 4], causing a surge in research interest. As part of their work on a modified capillary model to predict NF membrane performance, Soltanieh and Mousavi [5], for instance, investigated the application of bipolar NF membranes for water softening. Likewise, Bodzek et al. [6] looked into the softening of well and tap water using the DS-5-DK NF membrane and DS-3-SE RO membrane from Osmonics, and demonstrated that the NF membrane was more suitable for softening given its higher permeability. Ghizellaoui et al. [7] later studied the application of NF for partial softening of very hard water in Algeria, and concluded that NF was of great interest to the process. More recent works from Galanakis et al. [8] and Elazhar et al. [9] demonstrate that NF softening continues to be of interest as a process.

Apart from traditional softening applications, NF desalination pretreatment has lately been gaining momentum as evident from a recent review on integrated/hybrid membrane processes in desalination and water treatment by Ang et al. [10]. The review cites evidence that NF desalination pretreatment not only improves desalination feeds by reducing scaling, but also allows seawater reverse osmosis (SWRO) to run at lower pressures and potentially achieve higher recoveries [10]. In search of the optimal conditions for NF/SWRO desalination, Park et al. followed with their study on NF pretreatment and its effect on SWRO recovery under different conditions, and concluded that the NF/SWRO configuration featured an improvement in the quality of recovered water, especially at high recoveries [11].

1.2 Development of Novel Low-Pressure Nanofiltration Membranes

As becomes apparent from Bergman's cost analysis of softening technologies, however, one primary limitation on the economic viability of the NF pretreatment system has been the additional energy penalty incurred by the process [4]. Consequently, the requirement of lower energy consumption has occupied membrane researchers and

process designers alike in search of better separation efficacy.

While most NF membranes have been thin film composite (TFC) flat sheet membranes, a novel class of low-pressure NF hollow fiber membranes developed recently by layer-by-layer (LbL) polyelectrolyte deposition with chemical cross-linking appear to provide a solution [12, 13]. According to performance tests reported by Chang et al. [13], the newly developed membrane fared well when compared to state-of-the-art in softening and possessed superior softening performance compared to commercial NF membranes, such as NF 270 and NF 90, when operating at pressures that did not exceed 5 bar. These results prove the membrane's potential, raising research interest for potential large-scale implementation.

Despite their great potential, further progress on scale-up implementation of these or other NF hollow fiber membranes is restrained by the lack of information on large-scale or commercial NF hollow fiber modules, which is necessary to evaluate a membrane's potential for scaling-up. In this work, we develop the first mathematical model of the performance of NF hollow fiber modules on the system-level, building from experiments run on a bench-scale setup. To accurately predict streamwise variations that will be inherent in large-scale applications, the model takes a deeper look into the fundamentals governing fluid flow and mass transfer in hollow fiber modules, building from five decades of literature on hollow fiber modules and their modeling.

1.3 Modeling Hollow Fiber Membrane Modules

Since they were first patented in 1966 by DOW Chemical Company [14] followed by DuPont [15], research and development on hollow fiber membrane modules has made significant progress. A recent review by Peng et al. on state-of-the-art polymeric hollow fiber membranes highlights the major fabrication developments in the field over the past 50 years [16]. Hollow fiber modules have become attractive from an application standpoint given their desirable mass transfer characteristics and high surface area to volume ratio, which could reasonably reach 10 times that of a spiral-wound module [17]. Consequently, these modules have found applications across

a broad spectrum of fields, ranging from desalination and water treatment to gas separation, hemodialysis, blood fraction, and hydrocarbon separation [18].

The first attempts to model these systems were reported in the early 1970's with the works of Hermans [19] and Gill and Bansal [20] on RO hollow fiber modules. These authors, making use of the free surface model employed earlier by Happel to model viscous flow over arrays of cylinders [21], developed their models based on first principles, namely two dimensional mass and momentum conservation equations. Gill and Bansal's model fell short of accurately predicting the permeate concentration when validated with radial flow experiments [22]. This limitation, attributed to the assumption of constant membrane rejection underlying their model, paved the way later for an improved model that incorporated a diffusion model to describe solute transport [23]. As earlier models assumed negligible concentration polarization, Ohya et al. extended the analysis by developing a model to characterize the membranes used in the B-9 module by DuPont, and estimate their corresponding mass transfer coefficients [24].

Hermans afterwards introduced a simplified engineering model for hollow fiber module design by invoking several approximations, such as treating the membrane as a porous mass and assuming Poiseuille flow on the fiber bore-side [25]. A major shift in modeling literature later came from Bruining, who presented the first general model that rid itself from the traditional approach that solved the Navier-Stokes equations using perturbation analysis, power series, or numerical methods, and used simpler mass and momentum balances instead [26]. Taking into consideration the effects of concentration polarization and axial variation in hydraulic and osmotic pressures on permeate flux, Sekino later introduced the friction-concentration polarization (FCP) model for RO hollow fiber modules [27, 28], while Gooding and Alexander extended similar modeling capabilities to UF hollow fiber modules [29].

In spite of these developments in modeling literature, it soon became apparent that the proposed models neglected the nonuniformity and randomness that characterize hollow fiber modules, which have been recently reviewed by Mat et al. [30]. Earlier models, which assumed a uniform fiber packing (staggered or parallel) and an even

flow distribution among them much like a shell-and-tube heat exchanger, were too idealistic at best, and research interest shifted towards more realistic scenarios. In their study on shell-side feed modules, for instance, Park and Chang proposed a numerical model by combining the characteristics of wall jet and manifold flow [31]. Their modeling results, backed by experimental data, revealed that there exists a significant degree of nonuniformity in flow distribution among the fibers that affects the module efficiency, and depends on the module operating conditions.

Driven by this movement in literature, Wickramasinghe et al. [32], and later Elmore and Lipscomb [33], implemented a mass transfer model for hollow fiber geometries, assuming unequal fiber radii that vary according to a Gaussian distribution, to conclude that polydisperse hollow fibers produce uneven flows that could undermine the average mass transfer coefficient of a module. To model this randomness and assess its influence on module performance, Chen and Hlavacek were the first to apply Voronoi tessellation to randomly packed hollow fiber bundles [34]. While their approach presented a significant improvement, its underlying assumption of a uniform probability function for all modules makes it difficult to capture the varying degrees of packing irregularity possible under the same packing density [35]. In response, Zhang, more recently, introduced a method based on fractal theory to approach the problem of non-uniformity and randomness in fiber packing [35].

These RO/UF hollow fiber modeling efforts still remain unsuitable for NF, whose performance modeling requires radically more challenging models. Unlike RO or UF, NF performance is governed by the interplay of different separation mechanisms, namely sieving effects, Donnan partitioning, and dielectric exclusion. Unfortunately, modeling difficulty is compounded with the introduction of multi-ionic mixtures, which are of particular interest to softening and desalination applications [36], suggesting that any reliable model for NF hollow fiber modules must incorporate rigorous NF modeling.

1.4 Modeling Nanofiltration Membranes: A Review

In spite of the latest developments in NF low-pressure membranes, further progress demands a deeper understanding of the fundamentals underlying the NF process. Unfortunately, NF separation of multi-ionic solutions is often difficult to predict given the complex nature of the interactions that occur among the ions themselves, and the ions and the membrane [36]. A rigorous model becomes essential to understand what governs the separation process and what transport and membrane properties dictate the softening performance, before we can extend our NF softening capabilities even further.

Earlier studies on NF modeling, geared at softening applications, exemplify the challenges encountered in this area, and demonstrate the need for further investigation. In their work on bipolar softening membranes, Soltanieh and Mousavi [5] implemented a modified version of the two-dimensional capillary model. Their work, however, was specifically targeted at bipolar membranes and only investigated the solute rejection as a function of pH and polyelectrolyte concentration [5].

Bodzek et al. followed by looking into the application of both, the DS-5-DK NF membrane and the DS-3-SE RO membrane developed by Osmonics, to softening of well and tap water. Their results showed that NF, while being more permeable than RO, has sufficient selectivity and is more suited for softening applications [6]. In search of a deeper insight, however, Wesolowska et al. later extended this analysis by attempting to apply the DSPM-DE model to the DS-5-DK NF membrane only to conclude that the model cannot successfully be calibrated to real multi-ionic water solutions [37]. Results from these studies among others [36, 38], in addition to the recent developments in low-pressure softening membranes [12, 13, 39], underscore the pressing need for a comprehensive NF model applied to softening studies, featuring multi-ionic solutions at salinities approaching those of seawater.

Given the complexity associated with modeling transport and separation at a scale only one order of magnitude above atomic dimensions, NF modeling has been an active area of research for more than two decades. Since Tsuru et al. first proposed a

model based on the extended Nerst-Planck equation to describe NF [40], the majority of modeling accounts in literature have largely been based on this approach. Two such models, the space-charge pore (SCPM) model and the Teorell-Meyer-Sievers (TMS) model, were investigated for potential NF modeling by Wang and coworkers. The SCPM assumes a porous membrane with radial distribution of potential and concentration, and requires an efficient means of solving the Poisson-Boltzmann equation along with the extended Nerst-Planck equation. The TMS model, on the other hand, assumes a homogeneous membrane with a uniform distribution of potential and concentration [41].

Subsequently, Bowen and Mukhtar proposed a hybrid model (HM) that assumes a nonporous membrane, yet introduces hinderance factors to account for the hindered transport [42]. Later atomic force microscopy (AFM) results introduced by Bowen et al. proved the existence of discrete pores in NF membranes, suggesting that a porous model is more consistent. Based on the results they obtained by assuming a uniform distribution in the pores, nonetheless, Bowen et al. concluded that the additional complexity borne by the SCPM model is not justified, and the term "Donnan-Steric Pore Model" (DSPM) was first coined [43]. In spite of DSPM's great success with simple solutions such as that of uncharged solutes, dyes, and univalent electrolytes [44], its accuracy was challenged when applied to mixtures of electrolytes and multivalent ions [45]. Consequently, dielectric exclusion was later incorporated as a partitioning mechanism by Bowen et al. [46]. This paved the way for the development of the Donnan-Steric Pore Model with dielectric exclusion (DSPM-DE) by Bandini and Vezzani [47] and the open source program, NanoFiltran, by Geraldes and Alves [48].

Having been developed for bench-scale setups, these models' primary drawback, however, has been their inability to predict system-level performance or capture streamwise variations, which can be detrimental to module efficacy. In response, a recent study by Roy et al. targeted the development of comprehensive large-scale models for flat-sheet and spiral-wound NF modules, but did not consider NF hollow fiber modules [49]. The feasibility of operating at extremely low transmembrane pressures (TMP's) on the large-scale is not backed by empirical evidence, and still

appears questionable. Likewise, a commercial scale NF hollow fiber module for desalination and softening applications is not currently available, nor is a well-established procedure to design these systems. The problem is further exacerbated by the lack of a pragmatic approach to assess the viability of a specific hollow fiber membrane for such applications, and evaluate the effect different module dimensions and operating parameters can have on performance absent the need for expensive experimental procedures.

Despite the substantial efforts on modeling single salt solutions and ternary ionic mixtures, a subject fairly established and well understood in NF literature, very few studies specifically targeting multi-ionic mixtures, such as artificial seawater, currently exist. This shortcoming is exacerbated by the scarcity of results available on modeling softening, which are necessary for understanding and optimizing the process. Although significant progress has been made on the fabrication-front when it comes to the novel NF hollow fiber membranes introduced earlier [39, 12, 13], a lot remains to be done as no formal attempt has been made to model these membranes. The transport and partitioning mechanisms underlying their performance, in addition to what properties makes this new class of membranes particularly promising for softening, remain obscure. To the best of our knowledge, no specific efforts in literature have been made to investigate which of the membrane properties in the DSPM-DE model dominate a separation process, and what implications that could have on our understanding of low-pressure NF softening. These challenges combined underscore the need for further investigation in this area.

1.5 Research Objectives

In this work, the DSPM-DE model is adopted for the first time to predict the softening performance of the cross-linked LbL1.5C NF membrane, fabricated in-house. The objective is to provide and validate a rigorous approach to characterizing the membrane, offer a complete description of the softening process involved, and extend our current understanding of low-pressure NF softening. Experiments on uncharged

solutes, ternary ionic mixtures, and multi-ionic solutions, including artificial seawater, were carried out, and the resulting trends, including negative rejection, were investigated. The nature of the multi-ionic interactions among the ions themselves, and the ions and the membranes are elucidated for the different hard water feeds considered in the study. An approach based on sensitivity analysis is proposed to determine the membrane property that dominates the softening process. Our results show that the membrane effective pore size and pore dielectric constant (and surprisingly not the membrane charge density) are the two parameters that dominate the softening process for this membrane.

From there, we present the development of the first system-level model for NF hollow fiber modules, combining state-of-the-art NF modeling, based on the DSPM-DE model, with fundamental conservation laws that govern fluid flow and mass transfer in hollow fiber modules. Our next objective is to develop a model that enables designers to understand the physics underlying module performance, internalize the various trade-offs existing in module design, and assess the feasibility of a membrane for a specific application, absent the need for costly experimental procedures on the large-scale. To demonstrate the model's capabilities, a preliminary module design was proposed, and parametric studies were run for the newly developed LbL membrane to assess its viability for seawater desalination pretreatment. Specifically, the effect of hydraulic losses in the bore and shell-sides on performance, the tradeoff between the recovery ratio and permeate quality, as well as the efficacy of raising recovery by increasing module length were all investigated. An approach based on comparing the marginal increase in recovery to the marginal rise in TMP is employed to illustrate that raising TMP can improve energy efficiency in some conditions when operating under extremely low TMP's, and a preliminary procedure for module sizing, inspired from the insights developed in this work, is proposed.

THIS PAGE INTENTIONALLY LEFT BLANK

Chapter 2

Modeling Nanofiltration Membranes: Theoretical Background

To model the separation performance of nanofiltration membranes, transport inside the membrane as well as in the concentration polarization layers has to be considered as shown in Fig. 2-1. While a typical TFC membrane is composed of an active layer and a porous support layer, the membrane separation is dictated solely by its membrane active layer [17], and hence, the support layer can reasonably be ignored throughout our analysis. In addition to the membrane active layer, the occurrence of concentration polarization on the feed/membrane and membrane/permeate interfaces can also undermine the membrane performance must be considered.

In light of these requirements, we start our modeling approach by an account of the main equations that govern solute transport inside the membrane active layer based on the Donnan-Steric Pore Model with dielectric exclusion (DSPM-DE). We then move on to concentration polarization outside the active layer, and lay out an approach to account for its effects. Afterwards, our system of equations is closed with the incorporation of solute partitioning under electrochemical equilibrium. Finally, a brief overview of the discretization process necessary to numerically solve the system is provided.

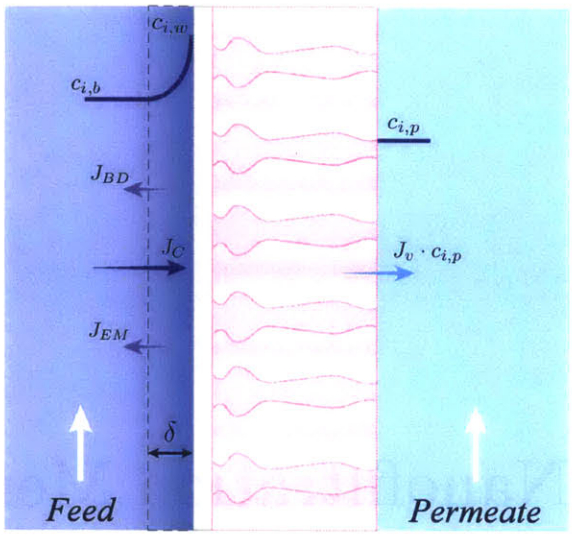

Figure 2-1: Schematic illustration of solute transport across a NF membrane.

2.1 Modeling Transport in the Membrane Active Layer

In the membrane active layer, the flux of the i^{th} solute, J_i, may be expressed in terms of the gradient in solute electrochemical potential as [46]:

$$J_i = -\frac{c_i D_{i,p}}{RT}\frac{d\mu_i}{dx} + K_{i,c} c_i J_v \tag{2.1}$$

$$D_{i,p} = K_{i,d} D_{i,\infty} \tag{2.2}$$

In Eq. 2.1, the solute electrochemical potential, assuming constant pressure and velocity in the pores, can be expressed as:

$$\mu_i = RT \ln a_i + z_i F \psi + \text{constant} \tag{2.3}$$

where a_i refers to the solute activity, respectively. By differentiating equation 2.3, and substituting the result back into equation 2.1, the extended Nerst-Planck equation is obtained [42]:

$$J_i = -D_{i,p}\frac{dc_i}{dx} + K_{i,c} c_i J_v - \frac{z_i c_i D_{i,p} F}{RT}\frac{d\psi}{dx} \tag{2.4}$$

The extended Nerst-Planck equation accounts for the transport of solutes through the membrane by diffusion, convection, and electromigration. The negative sign preceding the diffusive and electromigrative terms reminds us that transport through these mechanisms occurs down a gradient in concentration or electrical potential. Transport through convection, on the other hand, occurs as a result of the porous nature of NF membranes [43].

Given the scale of the pores in NF membranes, the mobility of the solutes through them is greatly reduced. The apparent rates of diffusion and convection are considerably lower in confining pores, relative to the bulk solution, when the pore and solute radii approach the same order. Under these circumstances, the transport is said to be "restricted" or "hindered" [50]. Hindered transport is accounted for in equations 2.1 and 2.4 through the inclusion of $K_{i,d}$ and $K_{i,c}$, which are hindrance factors for diffusion and convection, respectively. These factors are expressed in terms of the ratio of the solute Stokes radius to the pore radius, λ_i, and are related to the solute enhanced drag and lag drag coefficients as explained elsewhere [51]. For solutes with $\lambda_i \leq 0.95$, $K_{i,d}$ may be expressed according to the result obtained by Dechadilok and Deen [51]:

$$K_{i,d} = \frac{\begin{array}{c} 1.0 + (9/8)\lambda_i \ln(\lambda_i) - 1.56034\lambda_i + 0.528155\lambda_i^2 + 1.91521\lambda_i^3 \\ - 2.81903\lambda_i^4 + 0.270788\lambda_i^5 - 1.10115\lambda_i^6 - 0.435933\lambda_i^7 \end{array}}{(1-\lambda_i)^2} \tag{2.5}$$

For solutes with $\lambda_i > 0.95$, $K_{i,d}$ was calculated using the result obtained by Mavrovouniotis and Brenner [52]:

$$K_{i,d} = 0.984\left(\frac{1-\lambda_i}{\lambda_i}\right)^{5/2} \tag{2.6}$$

Similarly, $K_{i,c}$ was calculated using equation 2.7 according to this result by Ennis et al. [53]:

$$K_{i,c} = \frac{1 + 3.867\lambda_i - 1.907\lambda_i^2 - 0.834\lambda_i^3}{1 + 1.867\lambda_i - 0.741\lambda_i^2} \tag{2.7}$$

Although the hollow fiber membranes modeled in this study are cylindrical in geometry and not flat, Cartesian coordinates can still be invoked in the analysis with

reasonable accuracy under the condition that $\Delta x_e/d_o \ll 1$ [54], where Δx_e is the effective thickness of the membrane active layer and d_o is the fiber outside diameter. Apart from the extended Nerst-Planck equation, electroneutrality accounting for the membrane charge density X_d also needs to be satisfied:

$$X_d + \sum_{i=1}^{N} z_i c_i = 0 \tag{2.8}$$

2.2 Concentration Polarization and Mass Transfer Modeling

Concentration polarization refers to the formation of concentration gradients on the membrane feed and permeate interfaces as different constituents of the feed solution permeate through the membrane at different rates. This change in concentrations at the membrane interfaces leads to a reduction in permeate flux and rejection ratios. Concentration polarization can occur at the feed/membrane interface given the membrane selectivity at the active layer, and at the membrane/permeate interface as the membrane contacts a permeate enriched in one of the feed solution components. This effect can be controlled by adjusting the velocities in the feed and permeate channels, among other techniques [55]. For most membrane processes with bulk fluid flow through the membrane, concentration polarization on the permeate side, which is usually dilutive in salt-selective membranes, may reasonably be neglected [17].

Concentration polarization on the feed/membrane interface was accounted for using the model developed by Geraldes and Afonso [56]. According to their model, the net flux of solute i is expressed as the sum of the fluxes due to back diffusion, convection, and electromigration, as illustrated in Fig. 2-1.

$$J_i = -k_{c,i}^{\bullet}(c_{i,m} - c_{i,b}) + J_v c_{i,m} - z_i c_{i,m} D_{i,\infty} \frac{F}{RT} \xi \tag{2.9}$$

where ξ refers to the electric potential gradient at the feed/membrane interface, $c_{i,m}$ is the solute concentration at the feed/membrane interface just outside the pores, and

$c_{i,b}$ is the bulk concentration, respectively. Under steady state operating conditions, the flux continuity equation for solute i may also be expressed in terms of the permeate concentration $c_{i,p}$:

$$J_i = J_v c_{i,p} \tag{2.10}$$

Note that the diffusive flux in equation 2.9 is expressed in terms of a mass transfer coefficient, $k^{\bullet}_{c,i}$, determined from conventional Sherwood number correlations, and corrected for the "suction effect" caused by membrane permeation at the interface through the inclusion of the flux-dependent correction factor, Ξ, as follows [56]:

$$k^{\bullet}_{c,i} = k_{c,i}\Xi \tag{2.11}$$

$$\Xi = \phi_i + (1 + 0.26\phi^{1.4})^{-1.7} \tag{2.12}$$

with $\phi_i = J_v/k_{c,i}$. The mass transfer coefficient, $k_{i,c}$, was evaluated using the Sherwood number correlation for laminar flow in a tube with fully developed velocity profile, and developing concentration profile [57]:

$$\mathrm{Sh}_i = 1.62\mathrm{Re}^{0.33}\mathrm{Sc}_i^{0.33}(d_i/L)^{0.33} \tag{2.13}$$

with Re being the flow Reynolds number, Sc_i the solute Schmidt number, d_i the fiber inside diameter, and L the length of the module.

In addition to the concentration polarization equations developed in this section, two electroneutrality conditions should also be met in the feed and permeate regions. The first of these conditions, equation 2.14, applies at the feed/membrane interface, while the second condition, equation 2.15, applies in the permeate region [48]. These conditions take the form:

$$\sum_{i=1}^{N} z_i c_{i,m} = 0 \tag{2.14}$$

$$\sum_{i=1}^{N} z_i c_{i,p} = 0 \tag{2.15}$$

2.3 Solute Partitioning at Electrochemical Equilibrium

While diffusive fluxes act to eliminate concentration gradients in bulk solutions, concentration gradients can still exist in "true equilibrium" across a selective medium under certain conditions, such as a charged membrane [58]. The difference in concentration between a membrane's pores and the bulk solution is commonly referred to as solute partitioning, and plays a significant role in a membrane's selectivity towards solutes. Two additional expressions are obtained from describing solute partitioning under electrochemical equilibrium at the feed/membrane and membrane/permeate interfaces. These expressions are obtained by setting the electrochemical potential equal on both sides of an interface. In this derivation, we will refer to the solution inside the pores with a prime and consider a general interface for convenience:

$$\mu_i = \mu_i' \tag{2.16}$$

Substituting our definition for the electrochemical potential from equation 2.3, and accounting for solute nonidealities through the introduction of an activity coefficient yields:

$$\frac{\gamma_i c_i}{(\gamma_i c_i)'} = \exp\left(-\frac{z_i F}{RT}\psi_D\right) \tag{2.17}$$

In equation 2.17, which resembles the Nerst Equation, ψ_D refers to the Donnan potential forming across the membrane at equilibrium [59, 58, 60]. The activity coefficient is calculated using Davies model, which relates γ_i to the solution ionic strength, I, through the semi-empirical relation [61, 62]:

$$\ln(\gamma_i) = -Az_i^2\left(\frac{\sqrt{I}}{1+\sqrt{I}} - bI\right) \tag{2.18}$$

$$I = \frac{1}{2}\sum_{i=1}^{N} z_i^2 c_i \tag{2.19}$$

where b is assigned a value of 0.3 herein. A is the temperature-dependent Debye–Hückel constant expressed as [62, 63]:

$$A = \left(\frac{\sqrt{2\pi N_A}}{\ln(10)}\right)\left(\frac{e_0^2}{4\pi\varepsilon_0\varepsilon_r kT}\right)^{3/2} \tag{2.20}$$

with N_A being Avogadro's number, e_0 the elementary charge, ε_0 the permittivity of vacuum, ε_r the solvent's dielectric constant or relative permittivity, and k the Boltzmann constant.

Apart from the Donnan exclusion/partitioning mechanism expressed in equation 2.17 and in agreement with Donnan theory, other solute partitioning mechanisms occur across a NF membrane for which equation 2.17 fails to account. Based on geometric [50] as well as thermodynamic arguments [64], equation 2.17 has been modified in literature through the introduction of a steric term, which accounts for sieving effects that arise as a result of the finite size of the solute relative to the pore, quantified by the parameter λ_i [44].

$$\frac{\gamma_i c_i}{(\gamma_i c_i)'} = \Phi_i \exp\left(-\frac{z_i F}{RT}\psi_D\right) \tag{2.21}$$

$$\Phi_i = (1-\lambda_i)^2 \tag{2.22}$$

In addition to sieving and Donnan effects, evidence from electrochemical studies in colloidal systems suggests that the solvent's dielectric constant is considerably reduced in the membrane's confining pores relative to the bulk solution [46]. This difference in dielectric constant between the bulk solution and the membrane pores presents a barrier to ion solvation into the pores, as predicted by Born model, which leads to a higher ion rejection ratio. This partitioning mechanism is referred to as dielectric exclusion, is indifferent to the ionic charge, and becomes more significant with increasing ion valency. The dielectric exclusion mechanism has been extensively investigated in literature [47, 65], and is incorporated into Eq. 2.21 by the introduction of a Born solvation coefficient, Φ_B, with ΔW_i being the solvation energy barrier

computed in accordance with Born model [60]:

$$\frac{\gamma_i c_i}{(\gamma_i c_i)'} = \Phi_i \Phi_B \exp\left(-\frac{z_i F}{RT}\psi_D\right) \tag{2.23}$$

$$\Phi_B = \exp\left(-\frac{\Delta W_i}{kT}\right) \tag{2.24}$$

$$\Delta W_i = \frac{z_i^2 e_0^2}{8\pi\varepsilon_0 r_i}\left(\frac{1}{\varepsilon_p} - \frac{1}{\varepsilon_b}\right) \tag{2.25}$$

where r_i is the solute Stokes radius, ε_p is the dielectric constant of the pore, and ε_b is the dielectric constant of the bulk solution.

Applying Eq. 2.23 to account for solute partitioning at the feed/membrane and membrane/feed interfaces, the two additional expressions necessary are obtained. These expressions act as "boundary conditions" on the membrane interfaces with the feed and permeate solutions, and become increasingly important when solving for the concentration profile across the membrane. In writing these expressions, we follow the notation presented by Geraldes and Alves [48], where Eq. 2.26 describes the partitioning as it occurs just inside and just outside the membrane at the feed/membrane interface, and Eq. 2.27 describes partitioning as it occurs just inside and just outside the membrane at the membrane/permeate interface (Fig. 2-2):

$$\frac{\gamma_{i,1} c_{i,1}}{(\gamma_{i,w} c_{i,w})} = \Phi_i \Phi_B \exp\left(-\frac{z_i F}{RT}\psi_{D,w}\right) \tag{2.26}$$

$$\frac{\gamma_{i,N} c_{i,N}}{(\gamma_{i,p} c_{i,p})} = \Phi_i \Phi_B \exp\left(-\frac{z_i F}{RT}\psi_{D,p}\right) \tag{2.27}$$

Implicit in this derivation has been the assumption of electrochemical equilibrium, which might appear to be in contradiction with the observation that a finite flux of ions is always being transported across the membrane. The equilibrium assumption derives its validity from a primary restriction inherent in membrane transport models. This restriction is related to the equilibrium assumption and the way it is applied only across the feed/membrane interface or the membrane/permeate interface, and not the entire membrane as one entity. Stated differently, the equilibrium assumption

contends that the fluids on both sides of the membrane are in equilibrium with the membrane itself. This assumption implies that the gradient in chemical potential across the membrane will have to be continuous at all points inside and outside the membrane for equilibrium to exist, which certainly is a reasonable assumption under steady-state operating conditions [17].

2.4 Membrane Discretization and Modeling

The expressions derived thus far represent the equations that govern the transport and partitioning of solutes across a NF membrane at steady-state operating conditions. A complete account of these phenomena is obtained when the membrane active layer is discretized into nodes, as illustrated in Fig. 2-2, and one extended Nerst-Planck equation is applied for every solute at every node. These equations are coupled with the concentration polarization equation and the boundary conditions derived from solute partitioning to form a closed system that is solved numerically. Our numerical approach is in tandem with that presented by Geraldes and Alves [48].

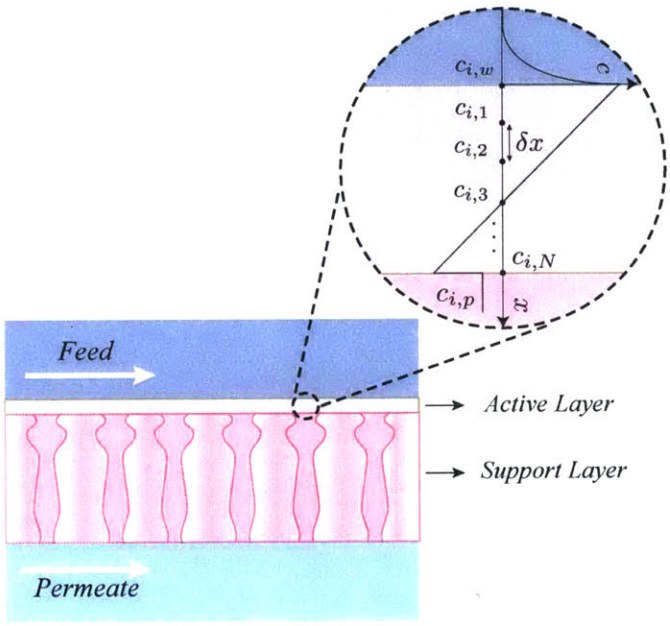

Figure 2-2: Modeling transport across a NF membrane.

THIS PAGE INTENTIONALLY LEFT BLANK

Chapter 3

Modeling Hollow Fiber Membrane Modules: Model Development

Generally, hollow fiber modules come in two main configurations, namely the shell-side feed and the bore-side feed configurations [17]. In the shell-side feed systems, similar to those developed by DuPont for RO, the pressurized process stream flows on the shell-side, as the permeate seeps through the membrane and flows on the inside of the fibers. Such a setup requires the incorporation of fibers with a relatively smaller diameter to sustain the large hydrostatic pressures imposed [17]. The bore-side feed configuration, on the other hand, features a process stream flowing inside the fibers with both ends open, while the permeate flows on the shell-side, respectively. Modules of this configuration typically have fibers of larger diameters to minimize pressure drops in the feed channel [17].

This work will focus on modeling the bore-side feed configuration, shown in Fig. 3-1, which was also the configuration adopted by Chang and coworkers in their work on the newly developed NF LbL membrane [12, 13]. According to Baker [17], concentration polarization is better controlled in this configuration as the occurrence of stagnant or dead zones, and feed channeling is avoided. Consequently, shell-side feed configurations are more prone to irreversible fouling as suspended particles find themselves trapped in these dead zones [17]. Furthermore, shell-side feed configurations often suffer from significant parasitic losses in the permeate channel, which

could considerably lower the driving force, and hence the permeate produced, across the membrane [17].

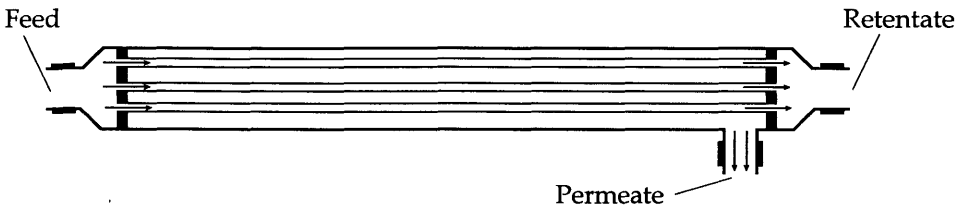

Figure 3-1: Schematic representation of the bore-side feed hollow fiber module configuration.

Apart from the difficulties associated with modeling NF separation of multi-ionic mixtures [56], developing a robust model for such a hollow fiber module is still a challenge in itself given the many "flow non-idealities" that are likely to arise in the system. According to Mat et al. [30], such non-idealities include flow maldistribution among the fibers even under uniform pressure and flow channeling, which could possibly arise from the random variability in fiber dimensions and non-uniform fiber packing. The criterion of uniform fiber properties and physical dimensions is particularly critical for the bore-side feed configuration as variations of even 10% can significantly deteriorate module performance [17]. These challenges add to the overall complexity of developing a descriptive model to completely describe the separation process; and as a result, adopting the right assumptions and approximations becomes pivotal.

In this chapter, the assumptions that underly the model are introduced and justified. Mass and momentum balances are applied, and a method to calculate the permeate flux as a function of the net driving force is proposed. The result is a system of conservation equations, while being strictly valid under the assumptions invoked, is still under-defined. As a result, we then introduce the DSPM-DE as a transport model to close the system and complete the analysis in the following chapter. Eventually, metrics to evaluate the module performance are presented, and a preliminary design for a NF hollow fiber module is proposed.

3.1 System-Level Modeling

The first stage involved in the modeling of a NF hollow fiber module is to analyze it at the system-level, through the application of mass and momentum balances. For the system at hand, feed water enters the module and is guided into the inside of the fibers as Fig. 3-1 illustrates. The result effectively is a division of the incoming feed stream among the numerous fibers in the module. We make the assumption that all fibers have uniform properties and dimensions, and are independent of one another. Accordingly, it follows that the process stream is divided equally among the fibers, allowing us to focus on an individual fiber. Within each fiber, the feed stream is processed in an inside-out filtration mode, such that the permeate is collected on the module's shell-side, respectively. Once the feed water reaches the end of the module, its concentration would have already increased, leaving the system as retentate. The permeate is also collected at the exit of the module as Fig. 3-1 shows.

3.1.1 Conservation Laws

To model the streamwise variations in the system, the fiber is divided into cells in the axial direction, as shown in Fig. 3-4a, and a backward finite-difference scheme is implemented. The boundaries of each cell form control volumes, illustrated in Fig. 3-4b, on which fundamental conservation laws can be applied. Conservation of mass can be applied to the different species forming the mixture. Applying conservation of mass to the solution on the feed and permeate sides yields:

$$\Delta Q_f = -J_v(\pi d_i)\Delta\ell \tag{3.1}$$

$$\Delta Q_p = J_v(\pi d_i)\Delta\ell \tag{3.2}$$

where Q_f and Q_p are the feed and permeate volumetric flow rates, J_v is the permeate flux, d_i is the fiber inside diameter, and $\Delta\ell$ is the step size or cell thickness, respectively. The opposing signs in Eqs. 3.1 and 3.2 imply that the mass lost in the feed must be gained by the permeate.

Equations 3.1 and 3.2 have been derived under the assumption of constant density as the solution flows from feed to permeate, so that mass conservation becomes equivalent to volume conservation. The validity of this assumption as it pertains to seawater is backed by empirical evidence showing that the density changes by less than 5% for reference salinities varying from 0 g/kg to 50 g/kg [66, 67]. The assumption is even more appropriate for NF membranes for which the density change is expected to be lower since mostly multivalent ions are separated from the solution. Experiments run on the NF LbL membrane, for instance, demonstrate that the membrane selectively rejects multivalent ions only.

Similarly, conservation of species can be applied to each of the ions or solutes present on the feed and permeate sides to arrive at:

$$\Delta \dot{N}_{i,f} = -J_v c_{i,p} (\pi d_i) \Delta \ell \tag{3.3}$$

$$\Delta \dot{N}_{i,p} = J_v c_{i,p} (\pi d_i) \Delta \ell \tag{3.4}$$

where $\dot{N}_{i,f}$ and $\dot{N}_{i,p}$ are the feed and permeate molar flow rates of solute i, and $c_{i,p}$ is the solute concentration in the permeate. The opposing signs in Eqs. 3.3 and 3.4 are obviously a manifestation of species conservation.

3.1.2 Permeate Flux and the Driving Force

To apply the mass balances, it is necessary to establish the link between the permeate flux, J_v, and the net driving force across the membrane. This can be accomplished using an empirical expression, introduced earlier by Bowen et al. for modeling NF membranes [44, 46]. The expression relates the flux to the effective driving force, $\Delta P - \Delta \Pi$, and membrane permeability:

$$J_v = \frac{r_p^2}{8\mu \Delta x_e} (\Delta P - \Delta \Pi) \tag{3.5}$$

where r_p is the membrane effective pore size, μ is the solution viscosity, Δx_e is the effective membrane thickness defined as the ratio of membrane thickness to porosity,

$\Delta x/A_k$, ΔP is the transmembrane pressure (TMP), and $\Delta\Pi$ is the osmotic pressure difference across the membrane. A detailed discussion of the different membrane parameters involved, and their method of estimation using the DSPM-DE model are covered in detail in this work, as well as in previous publications by Bowen and coworkers [44, 46, 68].

One major challenge imposed by Eq. 3.5 is computing ΔP and $\Delta\Pi$ as functions of position across the hollow fiber module. By accounting for the hydraulic losses, the transmembrane pressure can completely be expressed as:

$$\Delta P = P_f(\ell) - P_p(\ell) \tag{3.6}$$

$$P_f(\ell) = P_{f,in} - \Delta P_{f,L}(\ell) \tag{3.7}$$

$$P_p(\ell) = P_{p,in} - \Delta P_{p,L}(\ell) \tag{3.8}$$

where ℓ is the variable position in the axial direction, $P_f(\ell)$ and $P_p(\ell)$ are the inlet pressures, and $\Delta P_{f,L}(\ell)$ $\Delta P_{p,L}(\ell)$ are the hydraulic losses on the feed and permeate sides, respectively.

Assuming steady-state operating conditions and given the system setup, it is reasonable to expect the flow in the fibers to be laminar, and to assume $d_i/L \ll 1$ and $L/V_f \ll 1$, allowing us to approximate the flow as locally fully-developed [69]. Under this approximation, the pressure drop on the feed side can be expressed according to the Darcy–Weisbach equation [69, 70]:

$$\Delta P_{f,L}(\ell) = f_D \cdot \left(\frac{\ell}{d_i}\right) \cdot \left(\frac{\rho V_f^2}{2}\right) \tag{3.9}$$

$$f_D = \frac{64}{\mathrm{Re}} \tag{3.10}$$

$$\mathrm{Re} = \frac{\rho V_f d_i}{\mu} \tag{3.11}$$

with f_D being the Darcy friction factor, ρ the solution density, V_f the feed channel bulk velocity, and Re the flow Reynolds number. The pressure drop on the shell-side,

on the other hand, is more difficult to account for given the possibility of random fiber packing. According to the results reported by Zhang, who based his derivations on fractal theory, the Darcy friction factor in this case can be evaluated according to the correlations [35]:

$$f\mathrm{Re}_{D_h} = (-428.62\phi^3 + 620.49\phi^2 - 304.24\phi + 107.9)\Psi_f \tag{3.12}$$

$$\phi = N_f\left(\frac{d_i}{D_{i,module}}\right)^2 \tag{3.13}$$

$$\Psi_f = 1.149D_f - 1.0 \tag{3.14}$$

in which ϕ is the packing density, D_f is the fractal dimension, and Ψ_f is a correction factor that accounts for the randomness in fiber distribution at a given packing density. Inspired by earlier work on circle packing, Bezdek and Kuperberg proved in their work that the maximum packing density of congruent cylinders in space is $\pi/\sqrt{12} \approx 0.907$ [71]. According to Zhang, D_f approaches 1 for irregular packing, and 2 for regular packing; it ranges from $1.6-1.9$ for practical modules, respectively [35]. A value of $D_f = 1.7$ has been selected herein. D_h refers to the hydraulic diameter of the shell-side, and is evaluated in tandem with the definition used by Lipnizki and Field [72]:

$$D_h = \frac{4A_c}{P_w} = \frac{D_{i,module}^2 - N_f d_o^2}{D_{i,module} + N_f d_o} \tag{3.15}$$

with A_c being the flow cross-sectional area, P_w the wetted perimeter, $D_{i,module}$ the module inside diameter, and N_f the number of fibers in the module.

However, an attempt to implement these equations directly is counterproductive given the coupled nature of this problem. As shown in Fig. 3-2, the pressures on the feed and permeate sides, along with the permeate flux are all coupled parameters in this problem. The permeate flux, as expressed in Eq. 3.5, is a function of the net driving pressure; and as a result, will vary with the shell-side pressure. On the other hand, the shell-side pressure is also a function of the permeate flux. A greater permeate flux will lead to larger velocities in the permeate channel, resulting in greater

pressure drops on the shell-side according to the Darcy–Weisbach equation. By the same token, a greater permeate flux will lead to smaller velocities in the feed channel by conservation of mass, resulting in smaller pressure drops on the feed-side. This interconnected nature of the problem adds to the overall modeling complexity.

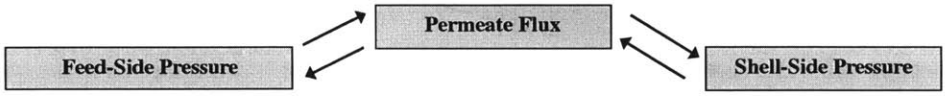

Figure 3-2: Coupled nature of the modeling problem.

While it could be argued a priori that the pressure drop on the permeate side will be negligible at low permeate flow rates [49], the validity of this assumption breaks down for hollow fiber systems, operating under considerably larger packing densities or high recovery ratios. In this work, we propose an iterative approach, represented in Fig. 3-3, to evaluate the pressure on the shell-side when simulating the module performance. According to Fig. 3-3, the process starts with an initial guess of the inlet pressure on the shell-side. From there, the model is solved sequentially for the permeate flux and flow rate in each cell, allowing us to estimate the pressure drop on the shell-side. Under the assumption that the permeate stream exits the system at atmospheric pressure, the initial guess for $P_{p,in}$ is then updated, and an error between both values is computed. This process continues until the error converges below a predetermined threshold, defined as ε_{set}. Using this iterative approach, we later show that the shell-side pressure drop is significantly smaller than the feed-side pressure under most operating conditions, and can reasonably be neglected, greatly simplifying the analysis.

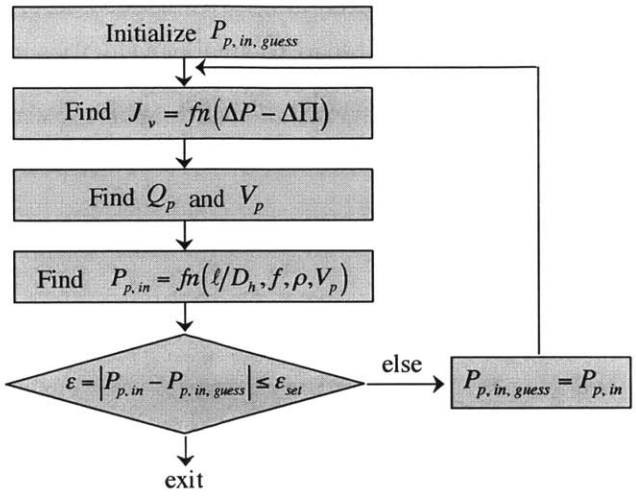

Figure 3-3: Proposed algorithm to the coupled problem.

In addition to computing ΔP, the osmotic pressure difference, $\Delta\Pi$, should also be computed for the permeate flux to be determined. The osmotic pressure difference, $\Delta\Pi$, is defined as [73]:

$$\Delta\Pi = \Pi_f - \Pi_p = \left(-\frac{RT}{V_S}\ln(a_S)\right)_f - \left(-\frac{RT}{V_S}\ln(a_S)\right)_p \tag{3.16}$$

where V_S is the solvent molar volume and a_S is the solvent activity in the solution. Under the assumption of dilute solutions, Eq. 3.16 can be approximated using van-'t Hoff's equation, which assumes a linear variation of osmotic pressure with concentration of the various dissolved ions [73]:

$$\Delta\Pi = \Pi_f - \Pi_p = RT\left(\sum_{i=1}^{N}(c_{i,f} - c_{i,p})\right) \tag{3.17}$$

Given that van 't Hoff's equation is valid for seawater concentrations [62, 73], and that osmotic pressure behaves as a colligative property under these conditions, the equation should still hold for slight variations from seawater concentrations and compositions. NF membranes generally, and the LbL membrane specifically, are mostly selective towards multivalent ions. Since the concentration of these ions is minor in the solution, the deviation from seawater concentrations caused by their retention

should also be minor.

While Eq. 3.17 completes our approach to system-level modeling, it presents yet another challenge by requiring the permeate concentration of each species, $c_{i,p}$, to be determined as a prerequisite. Since $c_{i,p}$ is a function of the membrane's selectivity, a membrane transport model is required as we explore next.

3.2 System-to-Local Level Modeling

In this work, the membrane transport model adopted has been the Donnan-Steric Pore Model with dielectric exclusion (DSPM-DE), whose fundamentals have been laid out previously in Chapter 2. Figure 3-4 summarizes the modeling approach presented in this work, and illustrates how the membrane transport model is coupled to the system-level analysis to provide a comprehensive model that can accurately predict the performance of a NF hollow fiber module under different operating conditions. The figure also reveals the necessary implementation of a two-dimensional discretization scheme (parallel + perpendicular to the fiber axial direction) for every solute, resulting in a three-dimensional matrix of unknowns, to solve the problem.

The integration of the well-validated DSPM-DE membrane transport model over the hollow fiber module not only completes the development of a model that can predict streamwise variations in system performance, but also opens the doors for design and optimization studies, and significantly alleviates the number of experiments necessary to predict system-level performance. Given the complexity and difficulty associated with predicting NF separation, such a model is essential to: (1) evaluate the performance of the hollow fiber configuration as applied recently to NF, (2) guide the scale-up implementation of the novel low-pressure NF membranes developed, such as the LbL membrane, and (3) assess the compatibility of a specific NF membrane with desalination pretreatment applications, absent the need for expensive large-scale experiments as we show in this study.

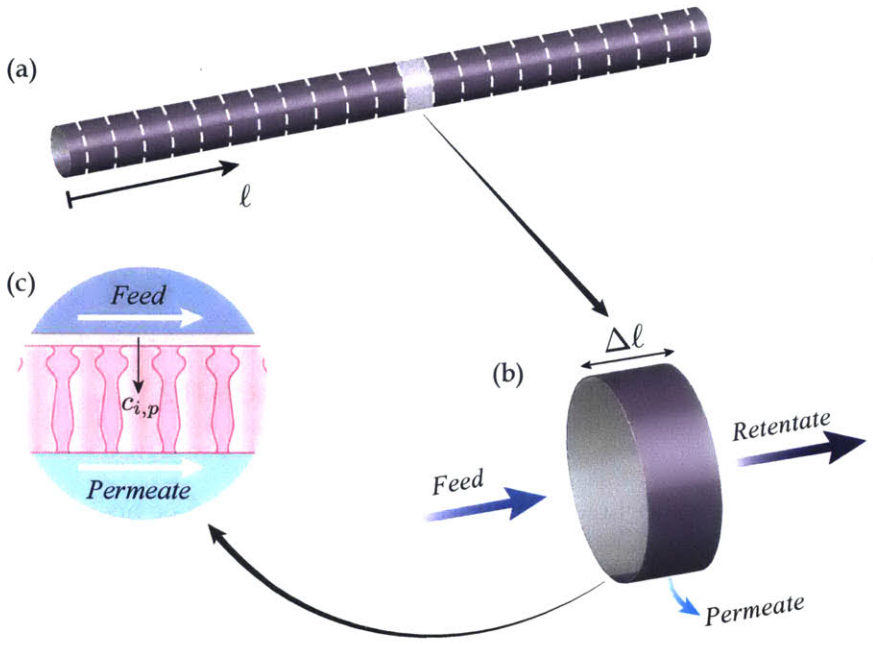

Figure 3-4: System-to-local level modeling: Modeling approach as applied to a single fiber to predict its separation performance.

3.3 Assessing Module Performance: Introducing Performance Metrics

In this section, we define the performance metrics used in this study. These metrics allow us to probe and quantify the effects different design parameters, and operating conditions could have on the system. Defined in Eq. 3.18, the membrane rejection ratio, R_i, measures the fraction of a solute that permeates through the membrane. The membrane rejection is a quantitative metric of the membrane's selectivity, and the quality of permeate produced. The system recovery ratio, RR, as defined in Eq. 3.19 measures the fraction of the permeate recovered from the process stream. For a given transmembrane pressure, a higher recovery ratio implies a higher membrane permeability and a greater system yield. The concentration polarization factor, CP_i,

provides a measure of the significance of concentration polarization under given operating conditions, and is defined in Eq. 3.20. Most importantly, the specific energy consumption, e, provides a metric to evaluate the energy cost of permeate production in the module, and is defined as in Eq 3.21.

$$R_i = 1 - \frac{c_{i,p}}{c_{i,b}} \tag{3.18}$$

$$RR = \frac{Q_{p,out}}{Q_{f,in}} \tag{3.19}$$

$$CP_i = \frac{c_{i,w}}{c_{i,b}} \tag{3.20}$$

$$e = \frac{Q_{f,in}\Delta P}{Q_{p,out}} = \frac{\Delta P}{RR} \tag{3.21}$$

3.4 Proposed Hollow Fiber Module Configuration: Module Sizing and Design

To proceed with system-level evaluation of module performance, a reference large-scale system needs to be adopted. Driven by the lack of commercial NF hollow fiber modules for softening and desalination pretreatment applications, we propose in this section a preliminary design inspired by earlier efforts on designing UF hollow fiber modules [74]. In spite of expected similarities, NF membranes are expected to depart from UF standards when it comes to the operating conditions, namely transmembrane pressure and feed flow rate. Since NF membranes have tighter pore sizes relative to UF, the transmembrane pressures are expected to be higher in NF. Driven by differences in the process streams UF and NF are designed to handle, UF hollow fibers will tend to have higher feed flow rates relative to NF to prevent membrane pore clogging. The specifications of the proposed design are summarized in Table 3.1.

Table 3.1: Nominal Specifications of Modeled Large-Scale Hollow Fiber Module

Specification	Nominal Value
Membrane Area	50 m^2
Module Length (L)	1.5 m
Module Outside Diameter ($D_{o,module}$)	165 mm
Packing Density (ϕ)	75%
Fiber Inside Diameter (d_i)	1 mm
Fiber Outside Diameter (d_o)	1.38 mm
Inlet Flow Rate (Q_{in})	600 L/h
Recovery Ratio (RR) at 3 bar	25-30 %

Similar to commercial UF hollow fiber modules, such as those developed by Dow [75] and Koch Membrane Systems [76], a total membrane area of 50 m^2 with a module length of 1.5 m, and an outside module diameter of 165 mm were selected. The corresponding packing density is 70%. Our modeling results show, as we demonstrate later, that the hydraulic losses in the system are minimized around that packing density. The fiber dimensions and operating pressures of the system have been set by constraints on the LbL deposited membranes, fabricated in-house [13]. Unless otherwise specified, the inlet flow rate has been matched for the system to reach a preset value of $25-30\%$ on recovery ratio, while ensuring the impact of concentration polarization on rejection is minimized. A too low recovery ratio undermines the economic feasibility of the system, while a too high recovery ratio presents challenges when it comes to fouling control and scaling prevention, especially with feeds akin to seawater. Given the scope of our work, the model feed was chosen to be artificial seawater when assessing large-scale module performance as we show later.

Chapter 4

Model Validation and Experimental Results

In this chapter, we discuss the experimental setup used, as well as the experiments ran to validate the model, characterize the membrane, and predict its performance. The chapter starts by describing the experimental setup used, as well as the set of experiments ran as part of this study. Thereafter, a membrane characterization approach, a prerequisite to any NF modeling, is presented. From there, model validation is discussed, in addition to the results and their implications on low-pressure NF. Eventually, a sensitivity analysis approach is presented to uncover which membrane characterisitic dominates the low-pressure membrane separation process.

4.1 Nanofiltration Performance Experiments

Performance experiments were ran on the bench scale cross-flow filtration setup, shown in Fig. 4-1. According to the figure, feed water is pumped through a bench-scale hollow fiber system, and later expanded back via an expansion valve for recirculation. Filtration experiments were conducted using uncharged solutes (200 ppm), single salts (1000 ppm NaCl / pH range: $5-9$), and salt mixtures ($NaCl+MgCl_2$, $NaCl+NaSO_4$, artificial seawater) in an inside-out filtration mode. Pressures varied from 1 to 4 bar, and a cross-flow velocity of 0.3 m/s was maintained. Results obtained

from three membrane modules were averaged before testing results were reported.

For uncharged solute experiments, the total organic carbon concentrations of the feed and permeate were measured using a TOC analyzer (TOC-VCSH, Shimadzu, Japan). The feed and permeate concentrations in single salt experiments were measured by conductivity measurements (Ultrameter II, Myron L Company, Canada). An inductively coupled plasma optical emission spectrometry device (ICP-OES, Optima 8000, Perkin Elmer, USA) was used to measure cation and sulfate concentrations in the feed and permeate solutions for mixed salt experiments.

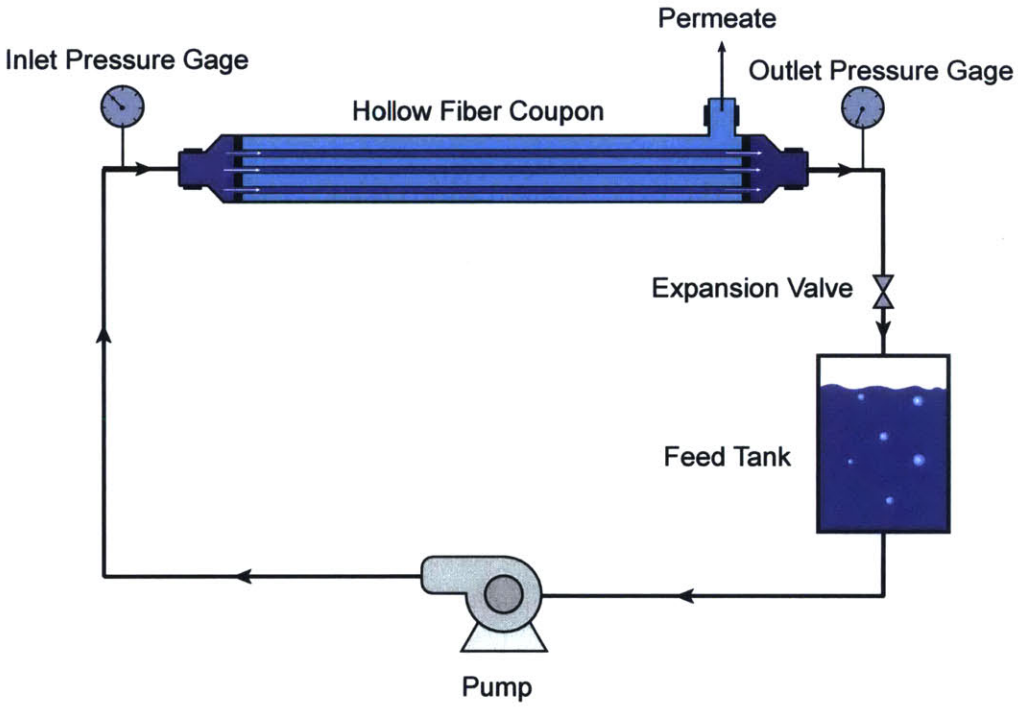

Figure 4-1: Cross-flow filtration unit used in running NF performance tests.

4.2 Membrane Characterization

One crucial aspect of membrane modeling involves characterizing the membrane in terms of parameters that allow it to be described with reasonable accuracy using simplified mathematical models. The process of membrane characterization in NF literature has undergone considerable changes over time as the models grew in so-

phistication. In the early nonporous hybrid model (HM) introduced by Bowen and Mukhtar, NF membranes were only characterized by two parameters, the effective membrane charge and thickness [42]. With the introduction of the porous DSPM model, the membrane effective pore size was then added and coupled with the effective membrane thickness through the Hagen-Poiseuille equation [43]. Realizing the importance of the process as a prerequisite to running any model, Bowen and Mohammad later developed a simplified characterization method, and applied it to 29 NF membranes from 10 manufacturers [68]. The membrane pore dielectric constant was eventually added to the list of membrane parameters to account for dielectric exclusion [46].

The membrane characterization approach adopted in this study was inspired by the earlier work of Bowen and Mohammad [44] and Bowen and Welfoot [46]. In our approach, a set of 4 experiments are necessary to accurately characterize the membrane. The effective membrane pore size and thickness are first determined from uncharged solute and pure water permeability experiments. These are followed by the membrane pore dielectric constant and effective membrane charge, which are determined from single salt experiments at different pH values, and mixed salt experiments. The solute properties used in this process and later in the study are summarized in Tables 4.1 and 4.2 for reference.

Table 4.1: Uncharged Solute Properties.

Solute	Molecular Weight (g/mol)	r_i (nm)	D_∞ ($m^2/s \times 10^{-9}$)
Atrazine	215	0.390	0.553
Gylcerol	92	0.260	0.950
Glucose	180	0.365	0.690
Sucrose	342	0.471	0.520
Xylose	150	0.300	0.769

Table 4.2: Charged Solute Properties.

Ion	Molecular Weight (g/mol)	r_i (nm)	D_∞ ($m^2/s \times 10^{-9}$)
Na^+	23	0.184	1.33
Ca^{+2}	40	0.309	0.792
Mg^{+2}	24	0.347	0.706
Cl^-	35	0.121	2.03
SO_4^{2-}	96	0.230	1.06

4.2.1 Defining an Effective Pore Size: Uncharged Solute Experiments

The first step in the membrane characterization process involves the estimation of an effective pore size. The approach presented in this section follows the one presented first by Bowen et al. [43], and relies on running rejection experiments on uncharged solutes. In their work, Bowen et al. derive a closed form expression for the real rejection of uncharged solutes that is only a function of the membrane effective pore size and thickness. The result they obtained took the form:

$$R_{real} = 1 - \frac{c_{i,p}}{c_{i,m}} = 1 - \frac{K_{i,c}\Phi_i}{1 - \exp(-\mathrm{Pe}_m)[1 - \Phi_i K_{i,c}]} \tag{4.1}$$

$$\mathrm{Pe}_m = \frac{K_{i,c}}{K_{i,d}} \frac{J_v \Delta x_e}{D_{i,\infty}} \tag{4.2}$$

where Pe_m is the Péclet number that compares the convective relative to diffusive transport through the pores. This expression takes into account concentration polarization by considering the feed concentration at the membrane interface $c_{i,m}$ to calculate the real rejection, rather than the observed rejection. By allowing the Péclet number to take on increasingly larger values and convection to dominate membrane transport, a new expression for rejection is obtained, called "limiting rejection":

$$R_{\mathrm{lim}} = 1 - K_{i,c}\Phi_i \tag{4.3}$$

Empirical evidence shows that uncharged solute rejection increases with increasing permeate flux as convection becomes more dominant, and the permeate becomes less concentrated. What equation 4.3 underscores is the fact that beyond a certain value for rejection, denoted by R_{lim}, increasing the flux does not contribute to increasing rejections. Beyond this point, any increase in convective transport is offset by the increasing concentration polarization and solute transport across the membrane. This phenomenon of limiting rejection will later be encountered in our study, and was also observed elsewhere as well [43, 46, 77].

For Eqs. 4.1 - 4.3 to be helpful in membrane characterization, experimental results obtained for "real rejections" are required before values for an effective pore size and thickness can be fitted. To minimize the impact of concentration polarization on the fluxes obtained in experiments, uncharged solute experiments were run on glycerol, glucose, and sucrose at low concentrations (200 ppm) and relatively high crossflow velocities (Re $\sim$ 400). Under this setup and the low pressures of interest, the resulting real and observed rejections would be very close. The results obtained from running uncharged solute experiments, while operating between 1 and 4 bar, are summarized in Table 4.3. With these results, an average pore size of 0.5 nm was estimated, along with the values of the effective membrane thickness fitted for each solute according to Eqs. 4.1 and 4.2. These results are provided in Table 4.4.

Since uncharged solute rejection is indifferent to dielectric exclusion and Donnan effects, the DSPM-DE model was run using the values reported in Table 4.4, assuming $X_d = 0$ and $\varepsilon_p = \varepsilon_b = 80.4$, under exceedingly larger values of permeate flux and crossflow velocity to estimate the "limiting rejection" of each solute. These results are plotted in Fig. 4-2 against the limiting rejection curve, which is defined by Eq. 4.3. The good agreement observed between the values obtained for limiting rejection using an effective pore size of 0.5 nm and the limiting rejection curve suggest that this pore size can be used as the effective membrane pore size for all subsequent analysis [44]. It should be noted, however, that successfully defining a membrane effective pore size does not guarantee the existence of such well-defined cylindrical pores in the membrane, nor does it imply the presence of a uniform pore size distribution

Table 4.3: Uncharged Solute Experimental Results.

Pressure Applied	1 bar	2 bar	3 bar	4 bar
Gylcerol Rejection (%)	11	15	19.5	29
Glucose Rejection (%)	74	77	83	83
Sucrose Rejection (%)	93	94	93	92

Table 4.4: Membrane Modeling Parameters.

Solute	λ_i	r_p (nm)	Δx_e (μm)
Gylcerol	0.520	0.5	1.6
Glucose	0.730	0.5	1.2
Sucrose	0.942	0.5	1.0

throughout it. Instead, defining an effective pore size only implies that the hindered transport of solutes across a given membrane is equivalent to their transport across pores of this effective size [42].

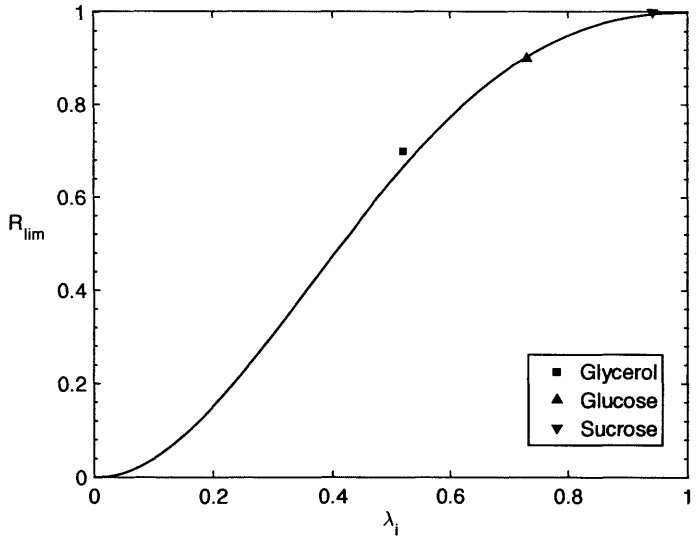

Figure 4-2: Plot of limiting rejection as a function of λ_i.

4.2.2 Defining an Effective Membrane Thickness: Pure Water Permeability Experiments

The membrane effective thickness, defined as the ratio of the membrane thickness Δx to its porosity A_k, can be estimated based on the Hagen-Poiseuille equation once an effective pore size is established [43, 68]. Assuming the pores are cylindrical and uniform in size, the permeate volumetric flux is given by:

$$J_v = \frac{r_p^2 \Delta P}{8\mu \Delta x_e} \tag{4.4}$$

with ΔP being the applied pressure, and μ the solution viscosity. Pure water permeability experiments, summarized in Fig. 4-3, provide evidence in support of a linear relationship between permeate flux and applied pressure. Given the value of r_p defined in Section 4.2.1 along with Eq. 4.4 and the experimental results in Fig. 4-3, the effective membrane thickness, Δx_e, was estimated to be 1.33 μm, agreeing closely with the results reported earlier in Table 4.4. Similar to r_p, this value of Δx_e will be assumed constant for all subsequent analysis in this study.

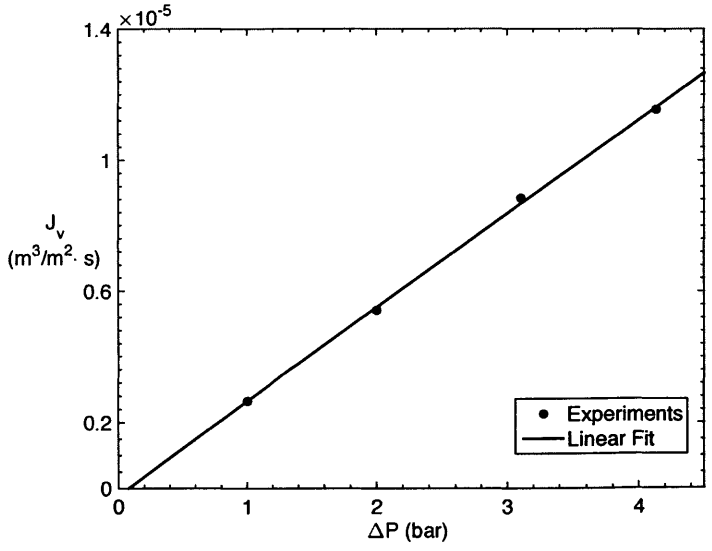

Figure 4-3: Pure water permeability (PWP) experiments for the LbL1.5C membrane.

4.2.3 Defining a Pore Dielectric Constant: Single Salt pH Experiments

Once the effective membrane pore size and thickness have been determined, the next step in membrane characterization involves estimating the membrane pore dielectric constant, ε_p. Fig. 4-4 illustrates the results obtained for the rejection of a 1000 ppm NaCl solution as a function of pH. As shown in the figure, the salt rejection initially decreases with increasing pH and reaches a minimum, before it starts increasing again. The point at which rejection is minimum is commonly referred to as the membrane "isoelectric point" (IEP), and is considered to be the point at which the membrane is uncharged [46]. Accordingly, this limits the membrane's partitioning mechanisms to steric partitioning and dielectric exclusion only, allowing for the pore dielectric constant to be determined using least squares fitting.

According to Fig. 4-4, the membrane IEP occurs between a pH of 7.0 and 8.0. To evaluate ε_p, least squares fitting was used to match the experimental results at a pH of 7.0 and 8.0, assuming the membrane is uncharged. The values obtained for ε_p from the analysis varied by less than 6% over this range. In this study, the IEP was taken at a pH of 7.0, which falls in line with the zeta-potential analysis carried on this membrane by Chang et al. [13], with its corresponding $\varepsilon_p = 41.3$, which will also stay constant for all subsequent analysis. To summarize, the DSPM-DE modeling parameters fitted for the LbL1.5C membrane from experimental results are listed in Table 4.5. This leaves only one degree of freedom, the membrane charge density, X_d, which will be our next subject of discussion.

Table 4.5: LbL1.5C DSPM-DE Paramters

Parameter	r_p (nm)	Δx_e (μm)	ε_p
	0.5	1.33	41.3

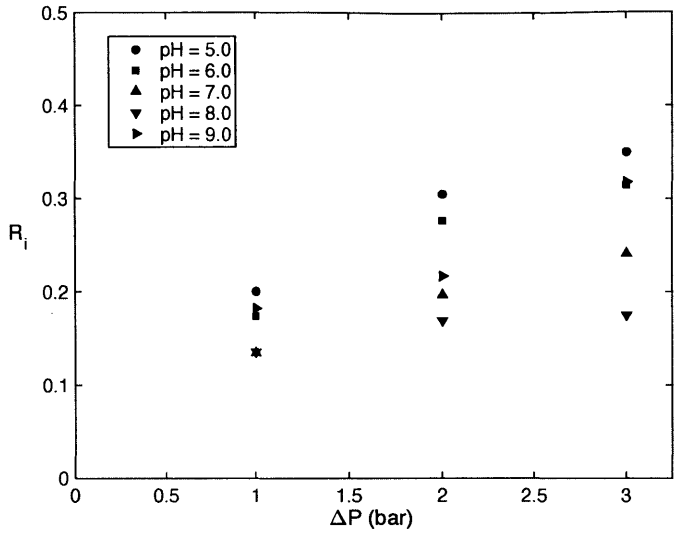

Figure 4-4: Rejection ratios as a function of applied pressure and pH for single salt experiments (1000 ppm NaCl).

4.2.4 Hard Water and Artificial Seawater Experiments

Estimating the membrane charge density, X_d, is the final stage of the membrane characterization process. Unfortunately, however, the membrane charge density is not only a function of the membrane, but is also sensitive to variation in feed composition and pH. Depending on the feed pH and composition, ion adsorption to the membrane [43] as well as dissociation of the membrane functional groups [78] could occur, ultimately affecting the membrane charge. In some instances, counterion adsorption has been reported, leading to complete shielding or even inversion of the membrane charge [79]. For these reasons, estimates of the membrane charge density are feed-specific at best. This leaves one degree of freedom when modeling any NF membrane using the DSPM-DE model. One way of handling this limitation has been the adoption of Freundlich isotherms, which express the membrane charge as a function of concentration based on empirical data [42, 44].

To study the softening performance of the LbL1.5C membrane and investigate its selectivity to various feeds, experiments were run on hard water of varying chemistries. The feeds examined, whose compositions are summarized in Table 4.6, include an

$NaCl+MgCl_2$ and an $NaCl+Na_2SO_4$ salt mixtures, in addition to an artificial seawater solution. The experimental results obtained for individual ion rejection and permeate flux as a function of applied pressure are listed in Tables 4.7 - 4.9. The estimated membrane charge density using least squares regression was $X_d = 2.83$ mol/m^3 for the $NaCl+MgCl_2$ mixture, $X_d = -1.92$ mol/m^3 for the $NaCl+NaSO_4$ mixture, and $X_d = -27$ mol/m^3 for the artificial seawater mixture, respectively.

Table 4.6: Synthetic Hard Water Feed Compositions.

Ion Concentration (ppm)					
Salt Mixture	Na^+	Ca^{+2}	Mg^{+2}	SO_4^{2-}	Cl^-
NaCl (1000 ppm) + $MgCl_2$ (1000 ppm)	398.6	–	254.2	–	1351
NaCl (1000 ppm) + Na_2SO_4 (1000 ppm)	718.7	–	–	678.2	606
Artificial Seawater (35000+ ppm)	11122	382	1394	2136	20300

Table 4.7: NaCl + $MgCl_2$ Observed Rejection Ratios.

NaCl + $MgCl_2$ Ion Rejection Ratios (%)				
Applied Pressure	Na^+	Mg^{+2}	Cl^-	Flux (LMH)
2 bar	−7.6	99.1	51.0	6.0
3 bar	−1.7	99.2	49.0	6.4
4 bar	1.6	99.0	51.0	6.6

Table 4.8: NaCl + Na_2SO_4 Observed Rejection Ratios.

NaCl + Na_2SO_4 Ion Rejection Ratios (%)				
Applied Pressure	Na^+	SO_4^{2-}	Cl^-	Flux (LMH)
2 bar	37.8	94.5	−9.0	7.1
3 bar	39.4	94.5	−7.0	7.7
4 bar	39.4	93.8	−6.0	7.9

Table 4.9: Seawater Experimental Rejection Ratios.

Artificial Seawater Ion Rejection Ratios (%)						
Applied Pressure	Na^{+}	Ca^{+2}	Mg^{+2}	SO_4^{2-}	Cl^{-}	Flux (LMH)
2 bar	−1.4	54.5	83.4	82.7	11	1.4
3 bar	−0.6	71.1	90.6	85.4	13	3.9
4 bar	1.17	78.9	93.6	86.8	15	6.0

4.3 Model Validation and Results

Characterization of the LbL1.5C membrane in the previous section sets the stage for validation of the DSPM-DE model and its applicability to this new class of low-pressure softening membranes. In this section, the DSPM-DE model is validated against the experimental results reported in Section 4.2 for uncharged and charged solutes. The observed trends, the underlying multi-ionic interactions, as well as insights obtained from the application of the model to the membrane are discussed.

4.3.1 Modeling Uncharged Solutes

To validate the model against uncharged solute experiments, modeling simulations were run while varying the pressures under which the membrane operates. The modeling results, which are illustrated in Fig. 4-5, had an average deviation of 12% from the experimental results, demonstrating excellent agreement between modeling and experimental results. As explained earlier, our modeling results in Fig. 4-5 capture how solute rejection increases with increasing flux, as convection dominates, until a limiting value for rejection is reached. Since the effective membrane pore size estimated (0.5 nm) was comparable to the Stokes radius of sucrose (0.471 nm), the model slightly overestimates its rejection. The results obtained also suggest that the LbL1.5C membrane is more selective towards glucose than glycerol, falling inline with the observation that glycerol has a smaller Stokes radius and a relatively larger

diffusivity according to Table 4.1.

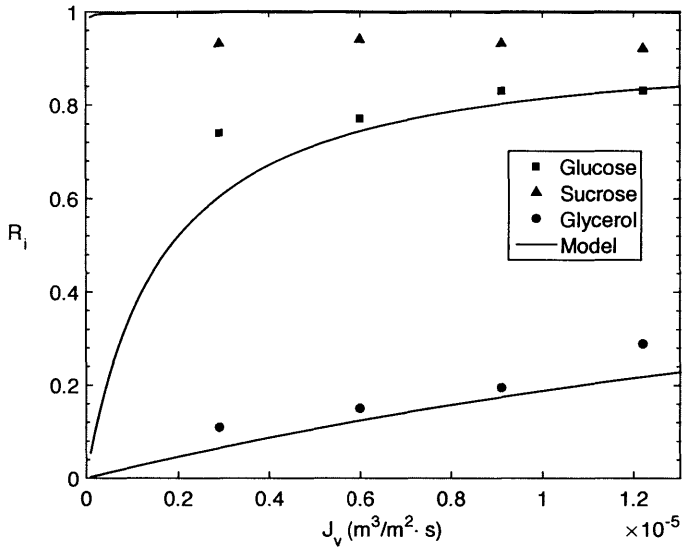

Figure 4-5: Experimental and modeled uncharged solute rejection as a function of applied pressure.

Following its validation, the model was run to predict the membrane's rejection to other solutes, namely atrazine and xylose, allowing us to investigate its performance over a wide spectrum of solutes. Similar to the results presented in Fig. 4-5, the obtained results reported in Fig. 4-6, demonstrate that the membrane selectivity towards uncharged solutes increases with increasing solute Stokes radius, or equivalently, decreasing solute diffusivity.

According to Table 4.1, the results in Fig. 4-6 suggest that solute rejection also increases with increasing molecular weight. Figure 4-7 underscores this fact by plotting rejection as a function of molecular weight. According to the figure, the uncharged solute rejection increases steadily with increasing molecular weight, and jumps once the solute Stokes radius approaches the effective membrane pore size ($\lambda_i \rightarrow 1$), before it slowly plateaus at 1. Using a plot similar to Fig. 4-7 along with a properly calibrated model allows for the molecular weight cut-off (MWCO) to be estimated without additional experimentation. For instance, the MWCO of the LbL1.5C membrane can be estimated to be approximately 250 Da, which is close to the MWCO of

205 Da reported experimentally by Chang et al. [13]. Since rejections are a function of permeate flux, an even closer estimate of MWCO = 215 Da can be obtained from Fig. 4-6.

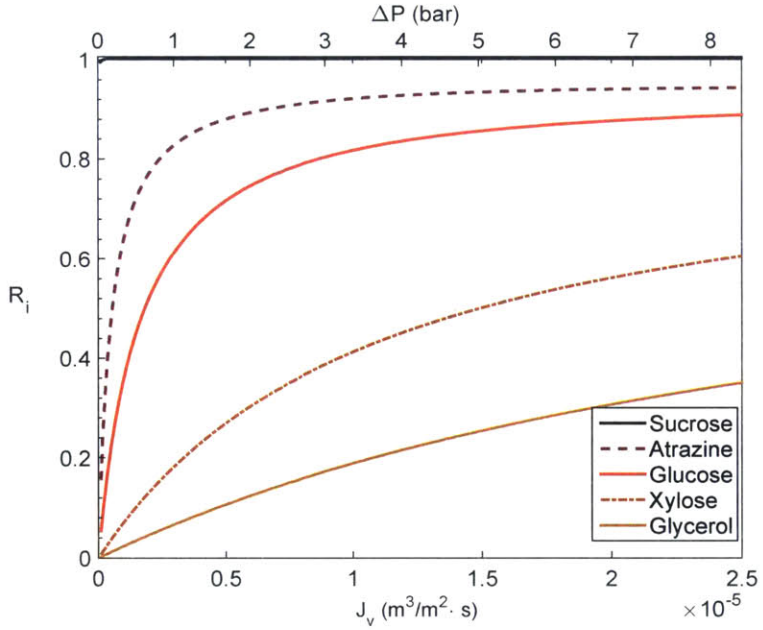

Figure 4-6: Predicting the LbL1.5C membrane performance for a variety of uncharged solutes as a function of applied pressure or permeate flux.

Since solutes are not perfect spheres, nor are membrane pores perfect cylinders, a plot similar to that in Fig. 4-7, while being qualitatively useful, should always be taken with scrutiny. Relying primarily on molecular weight to predict rejection could be misleading, for instance, should the solute deviate considerably from spherical geometry. Since solute rejection for uncharged solutes is primarily size-based, higher values of uncharged solute rejection would be achievable primarily with a tighter membrane, whose effective pore size is smaller.

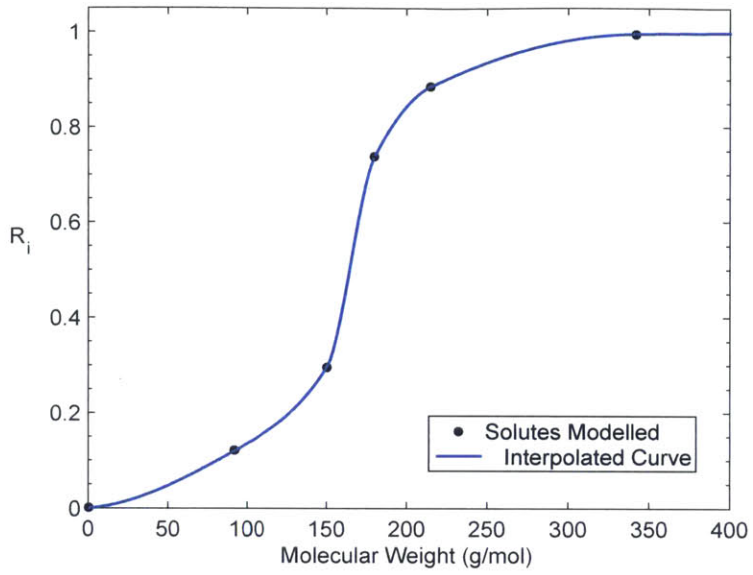

Figure 4-7: Plot of uncharged solute rejection as a function of solute molecular weight.

4.3.2 Modeling Hard Water Mixtures: The Phenomenon of Negative Rejection

Figure 4-8 shows the results obtained from modeling the NaCl+$MgCl_2$ hard water mixture, which strongly agrees with experimental results. With the introduction of charged species into the feed chemistry, the selectivity of the NF membrane is now a function of not only steric hindrance (size-based), but also Donnan partitioning and dielectric electric exclusion, adding to the overall complexity of the system. Similar to other results obtained for uncharged solutes, rejection increases with increasing flux for this mixture. The membrane has superior selectivity to the multivalent ion, Mg^{+2}, which is around 99% even at applied pressures as low as 2 bar. This high selectivity towards multivalent ions is a characteristic of NF membranes, and primarily governed by dielectric exclusion as our study proves later. Given that this is a ternary ion system, the interesting phenomenon of "negative rejection" is observed and is well-predicted by the model. This phenomenon has been encountered extensively in literature [42, 80, 81], primarily as a result of the interaction between the different pairs of coions in the solution and the membrane, as will become evident.

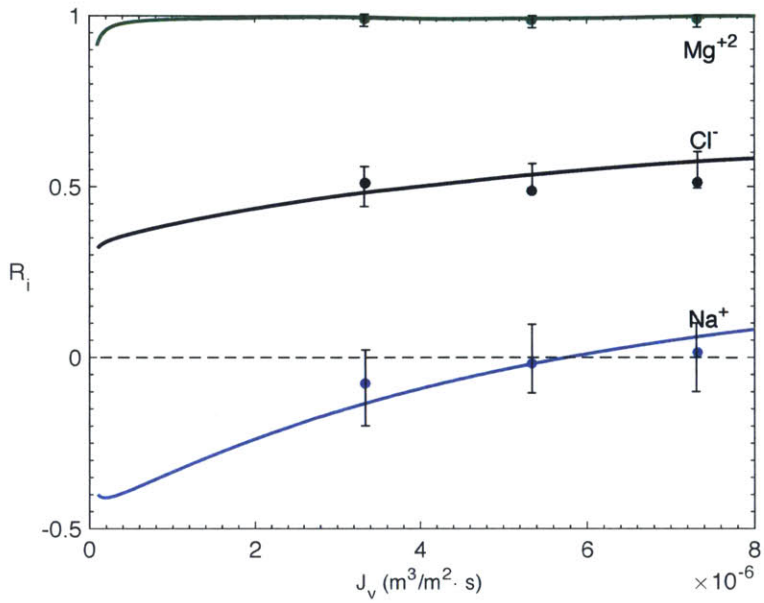

Figure 4-8: Experimental and modeling results for the rejection of the different ions in Mixture 1 as a function of permeate flux.

Fundamentally, negative rejection does not mean that mass (solute is this case) is being created, nor does it imply that the mixture now has more salts or ions than it initially started with. Negative rejection only implies that the system has a higher concentration of a given ion in the permeate, relative to the feed. In other words, negative rejection for a given ion species only occurs when more of that ion is in the smaller permeate volume relative to the much larger feed volume. The total number of ions is conserved, and only their relative allocation among the feed and permeate changes, primarily as a function of the membrane and ions in the solution.

Yaroshchuk provides a detailed account of negative rejection and the mechanisms that underly its occurrence [82]. These include equilibrium mechanisms, kinetic mechanisms, and a possible combination of the two. Based on our simulation results, which clearly indicate that the concentration of the negatively rejected ion unintuitively decreases in the membrane relative to the bulk, kinetic mechanisms must be responsible. Taking an example of a ternary system with two cations and one anion (similar to mixture 1), Yaroshchuk argues that negative rejection in this case results from the acceleration of the more mobile cation in the mixture. When dielectric exclusion starts

playing a more prominent role in solute partitioning, Yaroshchuk contends that a "relative pull-in" of the less charged coion could even result [82].

In light of this account, a physical interpretation for negative rejection in our case is reached by looking at the relevant transport mechanisms across the membrane in more detail. In the NaCl+$MgCl_2$ mixture, negative rejection of Na^+ cannot be a result of pure convective transport of the ions across the membrane. If we assume the membrane is completely passive towards to Na^+ (membrane does not see Na^+ to begin with), a lower bound of zero rejection will be observed. Zero rejection suggests that the membrane is passive (or indifferent) towards the Na^+ ions, and does not enhance nor restrict their transport, respectively. Since this is a lower bound, rejection cannot be lower; and hence, convective transport alone cannot be accountable, and does not explain the phenomenon. A similar analysis focused only on the diffusion of Na^+ leads to the same conclusion. Since diffusion acts to eradicate any concentration gradients across an interface, this transport mechanism cannot be responsible for reversing the concentration gradient, effectively making the permeate more concentrated than the feed. If neither convection nor diffusion of Na^+ can justify the negative rejection observed in experiments and predicted by our model, some other mechanism must be responsible.

The key point is the importance of the interaction between the different ions in the solution. On the feed side, the two cations, Na^+ and Mg^{+2}, are neutralized by the only anion in the mixture, Cl^-. This is consistent with the fact that the concentration of Cl^- exceeds that of Na^+ in the feed, as Table 4.6 shows. Driven by a gradient in electrochemical potential and a low rejection by the membrane, the Cl^- ions will diffuse from the feed to the permeate. Since the membrane is impermeable to Mg^{+2} by virtue of its selectivity (dielectric exclusion), the more mobile Na^+ ions are the only counterions available to neutralize the permeate solution. In effect, the diffusing Cl^- ions will "pull in" the extra Na^+ ions with them so that charge electroneutrality is always satisfied on both sides of the membrane. Stated differently, the transport of Na^+ ions is enhanced by the diffusing counterion, Cl^-, which leads to a higher concentration of Na^+ ions in the permeate and results in apparent negative rejection.

The same phenomenon was observed with the other hard water feeds studied, and a similar explanation applies to the trends seen.

A similar behavior was observed with the NaCl+$NaSO_4$ mixture as can be seen from Fig. 4-9. The membrane was has highly selective towards the multivalent ion, SO_4^{2-}, with rejection ratios close to 95% at applied pressures as low as 2 bar. This low operating pressure is possible given low membrane selectivity towards the monovalent ions, which constitute the majority of the mixture. Similar to the NaCl+$MgCl_2$ mixture, the more mobile coion, Cl^- in this case, is negatively rejected by the membrane. Given that the membrane is impermeable to SO_4^{2-} and that Cl^- is the only anion available to neutralize the transported Na^+ ions on the permeate side, the observation of negative rejection for Cl^- falls directly inline with our previous explanation.

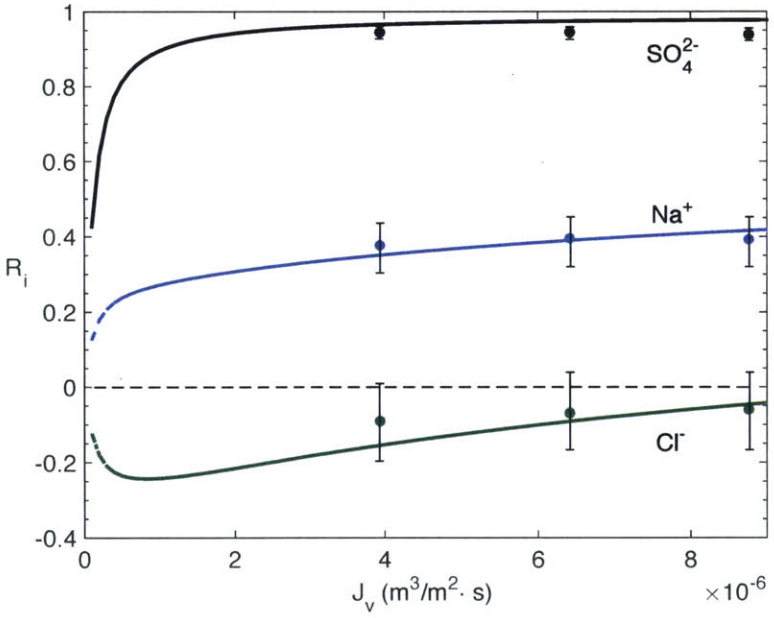

Figure 4-9: Experimental and modeling results for the rejection of the different ions in Mixture 2 as a function of permeate flux.

Rather than being indifferent to solute transport (zero rejection), a membrane with "negative rejection" essentially enhances the transport of that solute or ion across it. This ion is usually the more mobile coion in the mixture, and this phenomenon tends to be desirable when the target is to eliminate the less mobile ion (Mg^{+2} or SO_4^{2-}in this case). For softening applications specifically, rejection towards the multivalent

ions is the primary factor of interest. Being able to "selectively pick" the multivalent ions only, while intentionally allowing the monovalent ions to permeate, allows for softening to be carried out more economically, and at much lower energy penalties, as was observed with the LbL1.5C membrane (less separation work is necessary).

Another point to mention is the effect negative rejection could potentially have on the pumping work necessary to drive the separation process. The negative rejection of monovalent ions allows the permeate of the LbL1.5C to have a higher osmotic pressure relative to the permeate of other NF membranes that partially reject monovalent as well multivalent ions. This higher osmotic pressure on the permeate side reduces the osmotic pressure difference across the membrane, leading to lower applied pressures than otherwise would be necessary to reach the same permeate flux. Together, these two reasons elucidate the mechanics underlying low-pressure softening, and why this membrane fared well when compared to other commercial membranes in the experimental study by Chang et al. [13].

4.3.3 Modeling Artificial Seawater

Figure 4-10 shows the results obtained based on our model and experiments for artificial seawater. The high concentrations, the nature of the ionic interactions that occur among the ions themselves, along with the interactions between the ions and the membrane only add to the overall complexity of this system and provide a real challenge to the validity of the model and the assumptions involved. The agreement between the model and experiments is excellent, with a maximum deviation of 12% for the multivalent ions, showing the robustness of the model and characterization studies. As shown in Fig. 4-10, the membrane performs surprisingly well for softening, selectively separating only the multivalent ions while passing along the monovalent ions, keeping the osmotic pressure difference between the two streams at a minimum. As seen earlier, the rejection increases with flux until a limiting value is reached.

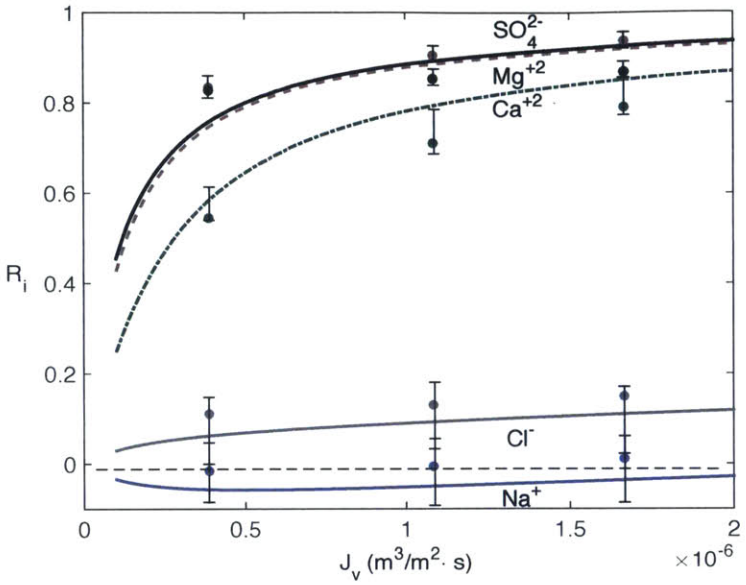

Figure 4-10: Experimental and modeling resulting for individual ion rejection ratio in artificial seawater as a function of applied pressure and permeate flux.

Although to a lesser extent, negative rejection still occurs in this system and can be explained by an account similar to that of hard water mixtures. To simplify our analysis to first approximation, we consider the membrane is impermeable to all multivalent ions, which include Mg^{+2}, Ca^{+2}, and SO_4^{2-}. On the feed side, the concentration of Cl^- exceeds that of all other ions in the system. Faced by the membrane's relatively low selectivity, Cl^- is transported from feed to permeate down its gradient in electrochemical potential. Na^+ is the only ion available to keep the permeate solution electroneutral; and as a result, an excess of Na^+ ions appears in the permeate relative to the feed, leading to negative rejection.

While this account explains rejection, and why Na^+ is rejected less than Cl^-, it falls short of explaining why the multivalent ions are rejected in this particular order. Focusing on the two multivalent cations, Mg^{+2} is rejected more than Ca^{+2} by virtue of its larger Stokes radius and lower diffusivity as shown in Table 4.2. Membrane charge becomes important when explaining why SO_4^{2-} is rejected at its current level. Being negatively charged under these feed conditions, the membrane rejects SO_4^{2-} more than Ca^{+2} by virtue of the resulting electrical interactions, in spite of sulfate's

lower Stokes radius and higher diffusivity compared to calcium. An analysis similar to ours could help elucidate the trends observed in other publications for NF rejection on feeds featuring multi-ionic solutions, which becomes increasingly important for NF applications in softening and desalination [11, 83].

4.4 Investigating the Membrane Selectivity: Sensitivity Analysis

In addition to our previous analysis on the LbL1.5C membrane, the DSPM-DE model enables us to probe what characteristics dominate the separation performance, expands our understanding of NF membranes, selectivity towards multivalent ions, and explains why this membrane specifically is superior when it comes to low-pressure softening. Although the high selectivity of NF membranes towards multivalent ions is well-documented in literature, no formal attempt has been made, to the best of our knowledge, to ascertain what mechanism or which membrane property is responsible for this very unique selectivity. In this section, we propose an approach based on sensitivity analysis to answer this question.

By taking any mixture from Table 4.6 as our model solution and running sensitivity analysis varying the membrane characteristics from their nominal values reported in Table 4.5 and Section 4.2.4, the characteristics that dictate the separation performance can be identified. The main assumption underlying this analysis is the independence of the membrane characteristics from one another, which is reasonable given the scope of this sensitivity analysis.

Figure 4-11 illustrates the results obtained from running such an analysis, assuming NaCl+$MgCl_2$ is the model solution and taking increments of 20% from the nominal values of each membrane parameter. These results suggest that the membrane softening performance is not a strong function of the effective thickness, or more surprisingly, membrane charge density in this case. In contrast, varying the membrane effective pore size or pore dielectric constant can have a dramatic impact

on softening performance, or multivalent ion retention, with greater dependence on the pore dielectric constant. Decreasing the membrane pore size makes the membrane relatively tighter, leading to higher rejections for any given flux. The increase in rejection, however, comes at an expense as the flux for any given pressure is expected to decline with a tighter membrane. Likewise, decreasing the pore dielectric constant also increases rejection as the ions experience a greater barrier to solvation, in accordance with the Born model.

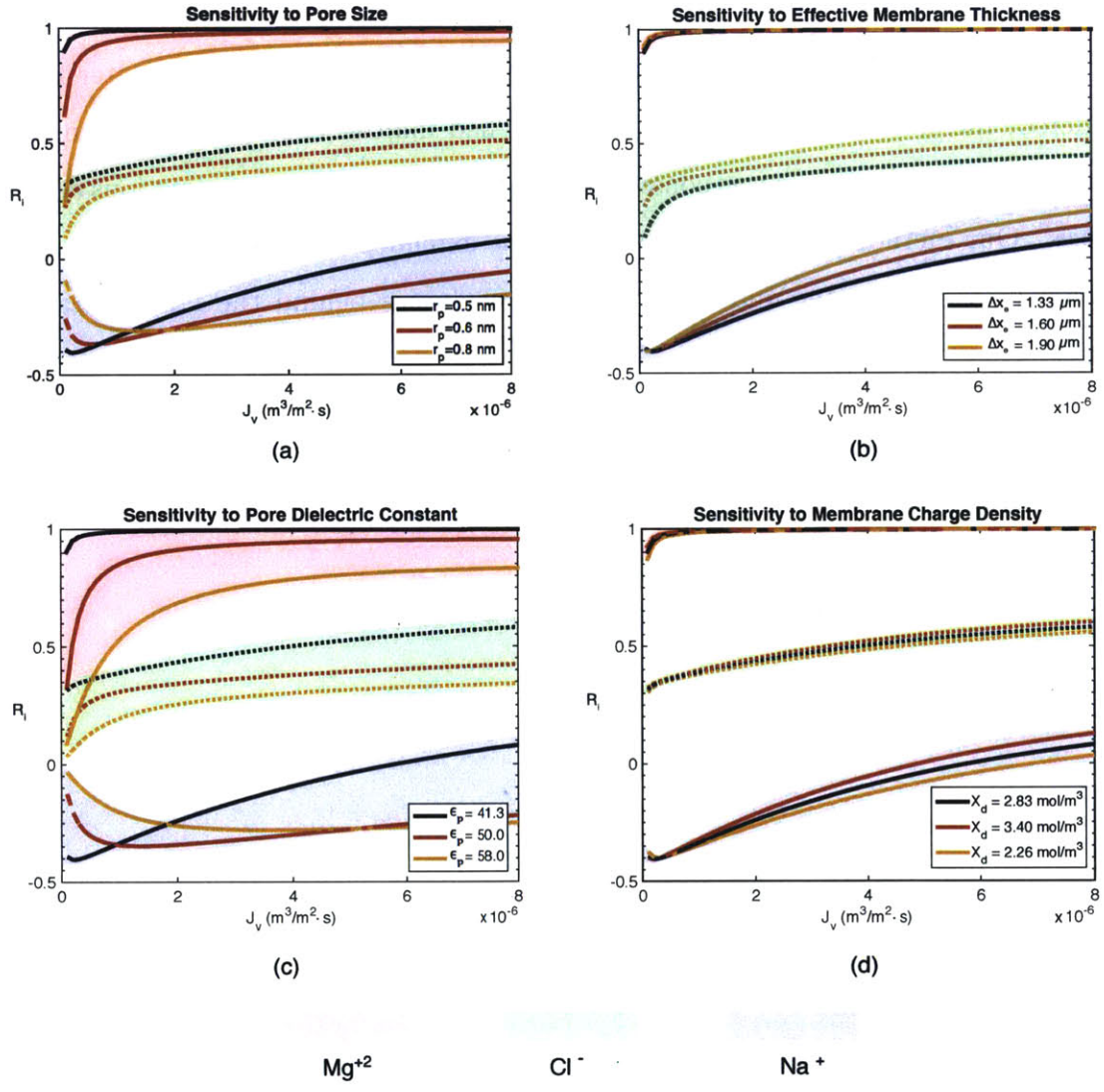

Figure 4-11: Results of the sensitivity analysis applied to the LbL1.5C membrane by varying: (a) the effective pore size; (b) the effective thickness; (c) the pore dielectric constant; and (d) the membrane charge density.

Similar trends have been observed when this analysis was extended to the other mixtures in the study. In all cases, the membrane pore dielectric constant played the biggest role, followed by the effective pore size, charge density, and finally the membrane thickness. These findings underscore the importance of dielectric exclusion and steric hindrance as partitioning mechanisms in softening applications, and indicate that it is the right combination of these properties that are mostly responsible for the observed softening performance.

The conclusion that the characteristic high selectivity towards multivalent ions of NF is not dominated by membrane charge, but by the pore dielectric constant and pore size, is backed by empirical evidence in our study. For all hard water feeds considered, including artificial seawater, which had multivalent cations and anions, the multivalent ion retention was consistently higher relative to monovalent ions across all cases. Our methodology could potentially be extended to other NF membranes, and help provide a better understanding of the physics behind the NF separation process.

Chapter 5

System-Level Modeling of Nanofiltration Hollow Fiber Modules

Parametric studies were run to investigate the effect of different parameters on module performance, and offer insights into module design. Specifically, the significance of module pressure drop, including bore-side and shell-side components, was assessed. The effect of feed flow rate on module performance was studied, and an optimal flow rate was observed. The importance of the developed model was underscored by the intensity of streamwise variations observed. Concentration polarization was examined under varying operating conditions.

More importantly, increasing module length to increase recovery was shown to be less effective under some scenarios, and leading to an interesting tradeoff between CAPEX and OPEX. A comparison of marginal increases in pressure to marginal increases in recovery is employed to show that raising pressure can have unexpected consequences when operating under very low transmembrane pressures (TMP's). This section is concluded with a simple design methodology to guide designers interested in extending the well-established hollow fiber configuration to nanofiltration.

5.1 Large-Scale Model Validation

Given the lack of experimental data on the performance of large-scale NF hollow fiber modules in literature, the developed model was validated with respect to experiments run on a bench-scale setup, using the LbL membrane, following the same procedure discussed in Chapter 4. To validate this model, the dimensions and specifications of the modeled system were scaled down to match those of the bench-scale setup, and simulations were run using the same hard water solutions investigated in Chapter 4. Excellent agreement is observed between the modeling and experimental results, validating the model for large-scale applications.

5.2 Module Pressure Drop

As part of their work investigating the effect of shell-side hydrodynamics on module performance, Costello et al. divided the shell-side pressure drop into a laminar component, which accounts for viscous drag along the fibers, and a turbulent component, which accounts for inertial drag due to stream splitting, channeling, and mixing [84]. Their results reveal a trend from "inertial-drag-dominated" to "viscous-drag-dominated" pressure drop with increasing packing density. The authors attribute this shift to the non-uniformity in fiber packing, suggesting that uniform packing is more likely at higher packing densities. They concluded that these results fall in line with the view that flow on the shell-side is three-dimensional, featuring bulk flow axially and transverse flow across the fibers due to channeling [84].

To assess the impact the permeate side pressure drop has on module performance in this case, a parametric study, looking into the module hydraulic losses as a function of the packing density and transmembrane pressure, was run. The results of this study are depicted in Fig. 5-1, showing the permeate-side and feed-side pressure drops as functions of packing density and transmembrane pressure, respectively.

As the results show, the hydraulic losses in the feed channel decrease as the packing density increases since the feed flow rate, $Q_{f,in}$, is now being divided among more

fibers, leading to lower velocities in each fiber. In contrast, the hydraulic losses on the shell-side increases with increasing packing density as the recovery ratio increases and hydraulic diameter gets smaller. This increasing shell-side pressure drop is similar in behavior to earlier results reported by Costello et al. [84]. Raising pressure has a similar effect by increasing the recovery ratio, which leads to higher hydraulic losses on the shell-side, and lower hydraulic losses on the feed-side. Figure 5-1 shows that these competing trends reach an optimum at around a packing density of 70%.

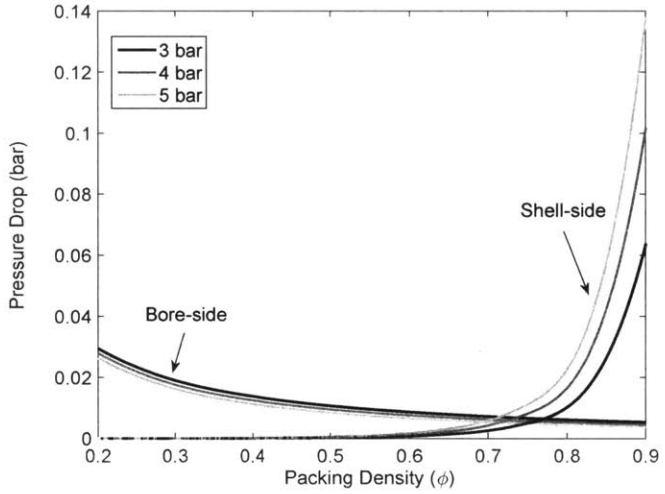

Figure 5-1: Bore-side (feed) and shell-side (permeate) hydraulic losses as a function of module packing density and transmembrane pressure (TMP).

Comparing the hydraulic losses to the transmembrane pressure applied reveals that the hydraulic losses are always a small fraction in this case. Figure 5-1 captures the fact that for reasonable packing densities ($\phi \leqslant 0.7$), the permeate-side pressure drop can indeed be assumed negligible given the low permeate velocities. Subsequently, we adopt this assumption in the model, which considerably lowers its computational expense.

5.3 Optimal Flow Rate

Solute rejection is the parameter of primary interest from a softening or pretreatment system design perspective as it quantifies the quality of water recovered from an initial

feed stream. At low feed flow rates, the feed concentration rises quickly, resulting in an increase in the osmotic pressure, and a corresponding decrease in permeate flux. Consequently, diffusion of solute species from the feed to the permeate becomes more dominant, and the permeate solution increases in concentration, ultimately reducing rejections.

To counteract this effect, which is primarily a manifestation of concentration polarization, feed flow rates need to be increased to raise mass transfer coefficients, and alleviate the rise in solute concentration along the module length. As a result, diffusive transport of species from feed to permeate is less encouraged, keeping the permeate concentration at a minimum, and ultimately increasing rejections.

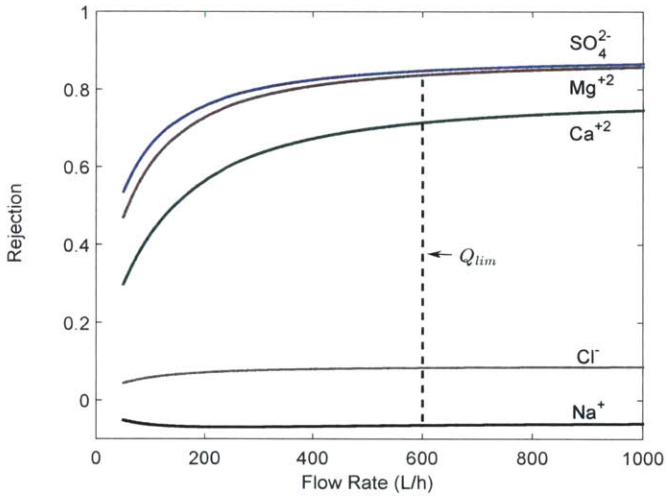

Figure 5-2: Module average rejection as a function of feed flow rate at a transmembrane pressure (TMP) of 3 bar.

To quantitatively capture this effect, Fig. 5-2 plots the observed rejection predicted as a function of the feed flow rate at a transmembrane pressure (TMP) of 3 bar. As the plot illustrates, the rejection increases with increasing flow rate, until a certain threshold, Q_{lim}, is reached. Q_{lim} is defined such that its corresponding rejection ratio is within 97% of the maximum obtainable at a flow rate of 1000 L/h. Increasing the feed flow rate beyond Q_{lim} does not increase rejection, but the energy penalty incurred from the increased pumping power continues to rise. To minimize the energy requirements associated with softening or pretreatment, while maintain-

ing high permeate quality, Q_{lim} represents the optimal flow rate at which the system should be operated for a given operating pressure. Similar trends were observed for higher operating pressures. Since the membrane is not selective towards monovalent ions, their rejection is not sensitive to changes in feed flow rates as Fig. 5-2 demonstrates.

5.4 Streamwise Variations

Another important aspect of system design is streamwise variations in module performance, which are not uncommon given the large-scale nature at which membrane treatment systems are implemented in practice. As the feed stream is processed along the module length, the bulk concentration of retained species in the feed channel rises. The resulting rise in feed osmotic pressure, coupled with the hydraulic losses incurred by the module, lead to decreasing rejections in the flow direction. A well-designed module should in practice be "balanced", meaning that streamwise variations from inlet to outlet are minimized, and the slopes at which the performance metrics vary per module are not steep. A well-balanced module has a relatively uniform flux, decreases the likelihood of fouling, suffers less from thermodynamic irreversibilities, and ensures the membrane area is utilized efficiently.

To magnify the magnitude of these variations, a parametric study was run by fixing the module flow rate at $Q_{f,in} = 300$ L/h, and varying the pressure from 3 bar to 5 bar, respectively. The results are shown in Figs. 5-3 and 5-4. Figure 5-3 plots the streamwise variations in feed bulk concentration as a function of length across the system. As the figure illustrates, streamwise variations become more significant with increasing transmembrane pressures, or equivalently increasing recovery ratios. For some ions, such as SO_4^{2-}, the concentration almost doubles from inlet to outlet, hinting at the detrimental effect streamwise variations could have on module performance.

Another point to elucidate is the order by which the concentration of the different ion species appears to be rising in the system. The trends observed are primarily a function of the selectivity of the LbL membrane. Since the membrane is not selective

towards monovalent ions, the concentrations of these ions appear to remain constant throughout the system. On the other hand, the order by which the concentration of the different multivalent ions rises stems directly from the selectivity of the membrane towards these ions. According to our previous results, the LbL membrane, confronted with artificial seawater, was highly selective towards SO_4^{2-} and Mg^{+2}, followed by Ca^{+2}. As Fig. 5-3 demonstrates, the concentration of SO_4^{2-} and Mg^{+2} rises the most since they are most strongly retained by the membrane.

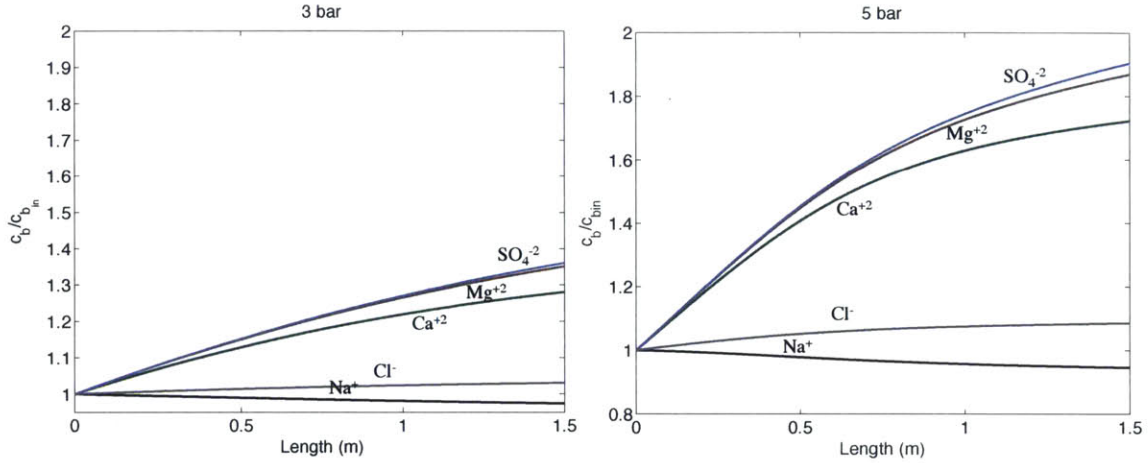

Figure 5-3: Streamwise variations in the feed bulk concentration at a feed flow rate of 300 L/h: (a) transmembrane pressure (TMP) of 3 bar; (b) transmembrane pressure (TMP) of 5 bar.

As with the feed bulk concentration, ion rejection is also a function of streamwise position. As shown in Fig. 5-4, the membrane retention of multivalent ions drops in the streamwise direction as a result of increasing ion diffusion across the membrane, and decreasing permeate flux. The membrane rejection of monovalent ions stays relatively constant given the membrane's lack of selectivity towards them. On the other hand, rejection drops for all multivalent ions, decreasing the most for Ca^{+2} since its membrane's selectivity is the least compared to the other multivalent ions present in the solution. Similar to Fig. 5-3, the decrease in multivalent ion rejection becomes more significant at higher transmembrane pressures, indicating that a rising bulk concentration, coupled with more prominent concentration polarization, acts to encourage ion transport across the membrane.

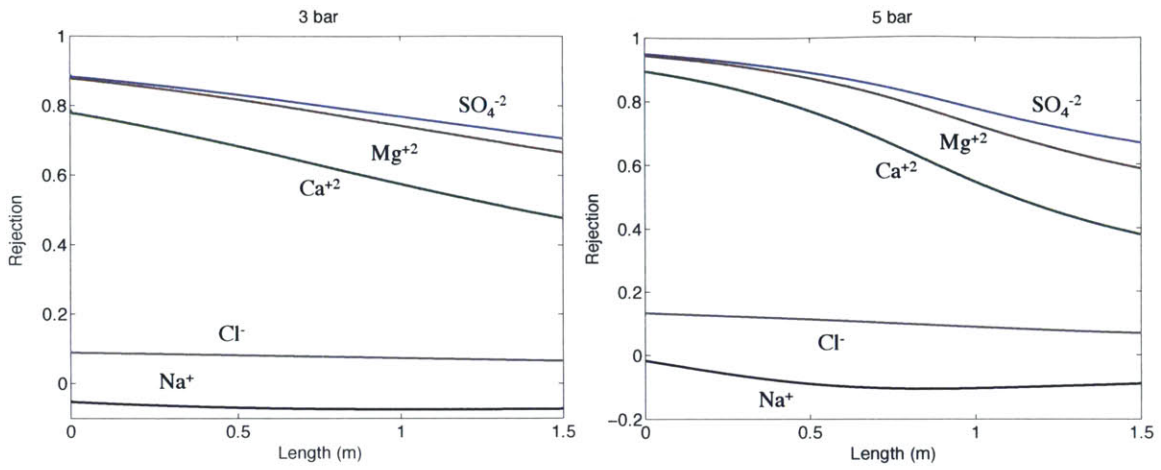

Figure 5-4: Streamwise variations in module rejection at a feed flow rate of 300 L/h: (a) transmembrane pressure (TMP) of 3 bar; (b) transmembrane pressure (TMP) of 5 bar.

The results discussed in this section underscore the importance of streamwise variations along the module, and their impact on overall performance. Another implication of the results presented is the apparent tradeoff a designer would face between module recovery ratio, RR, and rejection, R_i. While an improved system recovery is often desirable, a compromise might be necessary to ensure that an acceptable permeate quality is maintained. In the light of this discussion, concentration polarization emerges as an important variable in module design.

5.5 Concentration Polarization

Concentration polarization refers to the formation of concentration gradients at the membrane interface. From a design standpoint, concentration polarization is generally undesirable as it reduces permeate fluxes, and affects ion retentions. In this section, we investigate the magnitude of concentration polarization the proposed design is likely to experience during operation. The concentration polarization factor, CP_i, will be the primary metric used in this analysis. Similar to our approach in Section 5.4, the module flow rate was fixed at $Q_{f,in} = 300$ L/h to magnify the effect concentration polarization could potentially have on the system. The results of this analysis are

represented in Fig. 5-5.

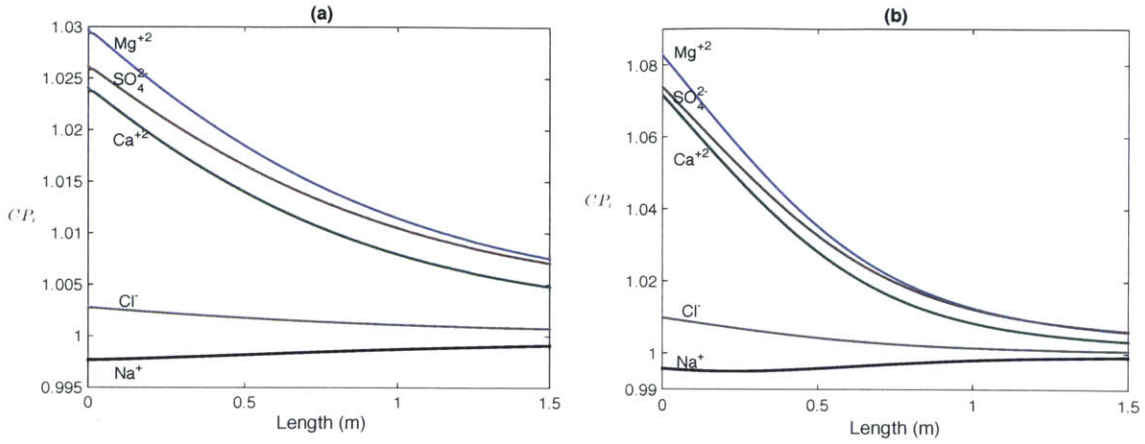

Figure 5-5: Streamwise variations in concentration polarization factor, CP_i, at a feed flow rate of 300 L/h: (a) transmembrane pressure (TMP) of 3 bar; (b) transmembrane pressure (TMP) of 5 bar.

Figure 5-5 depicts the streamwise variation in the concentration polarization factor across the system. Similar to Fig. 5-3, the order followed by the different ion species in the solution is primary a manifestation of the membrane's selectivity. The monovalent ions, which are not retained by the membrane, appear to experience no concentration polarization at all. In contrast, the multivalent ions SO_4^{2-} and Mg^{+2}, which are retained the most by the membrane, appear to experience the highest concentration polarization, followed by Ca^{+2}, as evident from the concentration polarization factor.

Another observation to point out is the growing role concentration polarization plays in the system as the transmembrane pressure increases. Interestingly, the concentration polarization factor for all retained species decreases across the length of the module. The decrease in the concentration polarization factor is primarily a result of the driving force, which diminishes across the module length as the osmotic pressure rises and the hydraulic losses accumulate. The result is a diminishing difference between the bulk and membrane concentration, respectively. Based on a heuristic from RO system design [17], the proposed module design appears to fare well when it comes to concentration polarization since CP_i did not exceed 1.1 in all cases. At higher flow rates, the effect of concentration polarization is expected to become even

less prominent.

5.6 Effect of Module Length

For a fixed feed flow rate, $Q_{f,in}$, two approaches are available to the designer to reach a specific recovery ratio, namely increasing the transmembrane pressure (TMP) or available membrane area in the system. In this section, we investigate both options by varying the transmembrane pressure and module length, or equivalently, the number of modules connected in series. The primary limitation on increasing membrane area is the declining driving force, $\Delta P - \Delta\Pi$, along the flow direction, which renders any increase in membrane area less effective at permeate recovery. In this study, the feed flow rate was fixed at $Q_{f,in} = 300$ L/h, and the resulting trends are reported in Fig. 5-6.

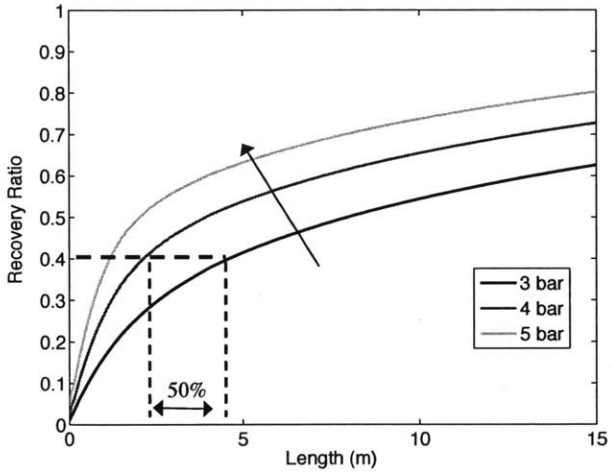

Figure 5-6: Effect of increasing module length and transmembrane pressure (TMP) on RR at a feed flow rate of 300 L/h.

According to Fig. 5-6, the recovery ratio increases with increasing transmembrane pressure and membrane area as expected. One important takeaway from this figure, however, is that the system length and its corresponding recovery ratio are nonlinearly related. Stated differently, doubling the number of modules present in the system does not double the resulting recovery ratios due to the drop in driving force or flux along

the length.

These results imply that while it might appear attractive to operate at lower pressures to lower the system's operational expenditure (OPEX), the additional capital expenditure (CAPEX) and OPEX from maintenance incurred by increasing the number of modules necessary to reach a specific recovery might be unjustified. For a fixed recovery ratio of 40%, for instance, our results demonstrate that raising pressure from 3 to 4 bar decreases the length required by approximately 50% as shown in Fig. 5-6. Consequently, a designer should take these considerations into account when searching for an optimal operating point for the system. In the next section, we present one approach to arrive at this optimal operating point by minimizing the specific energy consumed by the system.

5.7 Module Energy Consumption

Among all metrics considered in the study, energy consumption is perhaps of primary interest as it provides a handle on the energy penalty and carbon footprint associated with the NF process. In this section, the specific energy consumption, e, is chosen as the metric to evaluate the energy consumption of the proposed design. A set of parametric studies, whose results are summarized in Figs. 5-7 and 5-8, were run to investigate the dependence of the specific energy consumption on the transmembrane pressure and feed flow rate.

Figure 5-7 depicts the specific energy consumption of the system as a function of feed flow rate and transmembrane pressure. The results clearly indicate an increase in the specific energy consumption with increasing feed flow rate as more pumping work becomes necessary to drive the separation process. More surprisingly, however, these results suggest that the specific energy consumption decreases with increasing transmembrane pressure for all feed flow rates considered.

Another significant observation is that the increments of this decrease in e diminishes with increasing transmembrane pressures. Based on its definition, the only possible way e could decrease with increasing transmembrane pressures is for the re-

covery ratio, RR, to be growing at a much faster rate relative to the transmembrane pressure.

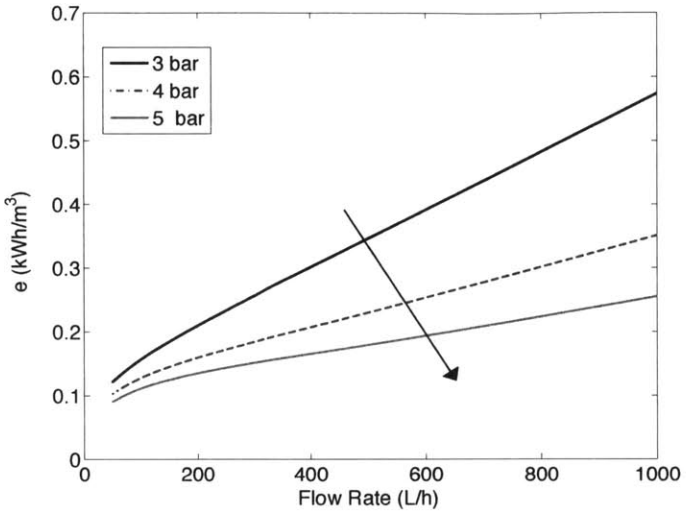

Figure 5-7: Specific energy consumption, e, as a function of inlet feed flow rate and transmembrane pressure (TMP).

To confirm this possibility, further simulations (Fig. 5-8) were run at the optimal feed flow rate defined earlier ($Q_{f,in}$ = 600 L/h). In accordance with the results presented in Section 5.3, the rejections of the multivalent ions at 600 L/h appear to be constant, indicating that increasing the module recovery ratios by raising the pressure does not have a major impact on the quality of permeate produced.

As shown in Fig. 5-8, the specific energy consumption initially decreases with increasing transmembrane pressure before reaching an optimal value, and then starts rising again. These results explain the trends observed earlier in Fig. 5-7, and indicate that the system initially benefits from raising the pressure since the marginal increase in permeate produced surpasses the marginal increase in transmembrane pressure. This trend, however, breaks down beyond the energy optimum, at which point the roles reverse and the marginal increase in pressure exceeds the marginal increase in permeate produced. This observation is further supported by the results reported in Table 5.1, showing that the rate of growth of the recovery ratio initially surpasses that of the transmembrane pressure before reaching the optimal point, respectively. Recently, similar trends of decreasing e with increasing RR in seawater NF have also

been observed empirically by Park and coworkers [11].

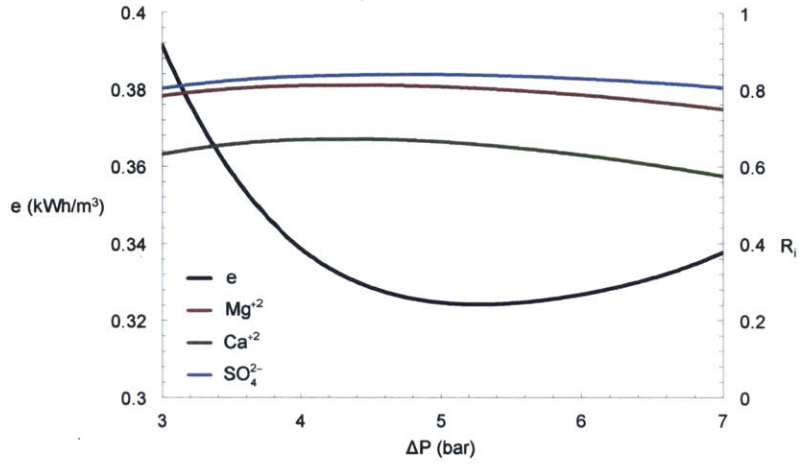

Figure 5-8: Specific energy consumption, e, and rejection, R_i, as a function of transmembrane pressure (TMP), at the optimal feed flow rate of 600 L/h.

Table 5.1: RR and e vs. Pressure

ΔP (bar)	RR	e (kWh/m^3)
3	0.2129	0.391
4	0.328	0.339
5	0.4278	0.325
6	0.51	0.327
7	0.5757	0.338

These results clearly indicate that operating at lower pressures, while it may appear attractive, could actually turn out to be more expensive, absent proper examination. The insights presented in this section underscore the importance of running an analysis similar to this work to evaluate the feasibility of a given membrane for system-level implementation in a specific application, or to help the designer locate an optimal point for operating the system.

These results clearly indicate that operating at lower pressures, while it may appear attractive, could actually turn out to be more expensive, absent proper examination. The insights presented in this section underscore the importance of running

an analysis similar to this work to evaluate the feasibility of a given membrane for system-level implementation in a specific application, or to help the designer locate an optimal point for operating the system.

We end this section by proposing a preliminary approach to designing a large-scale NF hollow fiber system for a given membrane, based on experiments run on a bench-scale setup. (1) A membrane needs to be characterized according to a specific membrane transport model. One approach has been explored in detail in our work on characterizing the LbL membrane based on the DSPM-DE model. (2) From there, the membrane should be modeled at the system-level in an analysis similar to the one developed in this work to locate an optimal feed flow rate. (3) Once an optimal feed flow rate is established, a set of parametric studies can be executed in search of an optimal operating point, at which the specific energy consumption is minimized. (4) Eventually, the initially proposed design can further be refined by running in-house experiments, coupled with sensitivity analysis and optimization studies using the proposed model.

THIS PAGE INTENTIONALLY LEFT BLANK

Chapter 6

Conclusions

In this work, the Donnan-Steric Pore Model with dielectric exclusion (DSPM-DE) was applied for the first time to model the performance of the novel LbL1.5C NF membrane, fabricated using layer-by-layer (LbL) deposition with chemical crosslinking. The objective of this study has been to extend our understanding of low-pressure NF as it applies to water softening, and to elucidate what makes the LbL1.5C membrane particularly suited for this application. To accurately model the membrane performance, several experiments were conducted on a wide spectrum of feed chemistries, ranging from uncharged solutes to single salts, salt mixtures, and artificial seawater.

The membrane has been characterized based on the DSPM-DE model, and modeling results were then validated with experimental results. The notable agreement between experimental and modeling results demonstrate the success of the model and the membrane characterization technique adopted. The modeling results were later used to explain the trends observed, and to elucidate the nature of the multi-ionic interactions that underly the membrane's selectivity, and in particular negative rejection. An approach based on sensitivity analysis was finally introduced to ascertain which membrane parameter dominates the high selectivity of NF membranes for multivalent ions, and dictate the superior softening capacity of the LbL1.5C membrane.

From there, a new system-level model for the NF hollow fiber membrane modules was developed based on an interdisciplinary approach featuring mass and momentum balances, coupled with the Donnan-Steric Pore Model with dielectric exclusion

(DSPM-DE) as the membrane transport model. The overarching object has been to present a model that, in spite of some approximations, empowers researchers and designers with: (1) an understanding of the physics that govern mass and momentum in the module, as well as the various tradeoffs that exist among design parameters and operating conditions; (2) a tool that predicts NF module performance under different operating conditions and complex feed chemistries, and enables membrane assessment for a given application, absent the need for costly large-scale experiments; and (3) criteria for module performance assessment along with a preliminary procedure for module sizing.

The model was validated against bench-scale experiments on the LbL membrane, a preliminary bore-side feed module design was proposed, and parametric studies were run to study the effect of different parameters on module performance. Specifically, the change in hydraulic losses on the bore and shell-side of the module with packing density and transmembrane pressure (TMP) were investigated, as well as the change in module average rejection as a function of feed flow rate. Streamwise variations in feed bulk concentration and rejection were observed, and the occurrence of concentration polarization was assessed. The tradeoffs between module rejection, recovery ratio, module flow rate, length, TMP, and specific energy consumption have been studied.

In summary, the main conclusions from this work can be divided into two sections, local-level low-pressure NF membrane modeling, and system-level modeling conclusions as we discuss next.

6.1 Local-Level Low-Pressure NF Membrane Modeling

In this work, local-level membrane modeling showed that solute retention increases with increasing permeate flux, until a limiting rejection value, characteristic of the solute and the membrane, is reached. Beyond this point, any increase in the solvent

convective transport is offset by the increasing solute transport. Solutes with greater retentions approached their limiting rejections at faster rates.

Uncharged solute rejection increased with increasing solute size, decreasing diffusivity, and increasing molecular weight, indicating that sieving effects dominated the separation process. A plot of uncharged solute rejection as a function of molecular weight can be used to estimate the MWCO of a NF membrane based on simulation results.

Negative rejection of the more mobile ion in a mixture, as observed in our softening experiments, is a result of kinetic effects, and stems from a relative acceleration of the negatively rejected ion, and the fundamental requirements of electroneutrality and zero electric current traveling through the membrane.

For artificial seawater, the sequence of multivalent ion rejection of the LbL1.5C was Mg^{+2}, SO_4^{2-}, Ca^{+2}, which is a result of the interplay between the ion's Stokes radius, diffusivity, and membrane charge.

Low-pressure NF softening is only possible as a result of a membrane's ability to selectively "pick" the multivalent ions out of the solution, while allowing monovalent ions to pass through by design. This characteristic eliminates the additional energy penalties incurred by the unnecessary separation of monovalent in addition to multivalent ions in softening.

Negative rejection of monovalent ions could prove advantageous in softening applications by increasing the osmotic pressure on the permeate side, leading to lower driving force requirements for a given permeate flux.

The selectivity of NF membranes towards multivalent ions is largely dominated by the pore dielectric constant. For the LbL1.5C, selectivity was dominated by the pore dielectric constant, followed by the pore size, charge density, and lastly membrane thickness.

6.2 System-Level Modeling

Modeling the NF hollow fiber modules at the system-level demonstrated that hydraulic losses increased on the shell-side and they decreased on the bore-side, as the recovery ratio was increased, and a crossover point was observed.

The magnitude of the hydraulic losses on the shell-side (permeate-side) was proven to be negligible relative to the TMP at low to moderate packing densities.

Module average rejection increased with increasing inlet feed flow rate as solute transport across the membrane decreased. The decrease in solute transport is a result of the diminished occurrence of concentration polarization, and the more spatially-uniform feed concentrations. The trends break down beyond a certain threshold, and an optimal feed flow rate was observed.

Streamwise variations in the feed bulk concentrations and rejection ratios were more prominent at higher TMP's; and the relative magnitude of these variations was proven to be a manifestation of the membrane selectivity towards their corresponding species.

With a decaying driving force across the module length, the difference between feed bulk concentration and wall concentration also decays, causing the concentration polarization factor to decrease in magnitude along the flow direction.

Employing larger membrane area to increase module recovery was shown to be less effective at low TMP's as the driving force decays along the module, making the additional membrane area less effective for permeate recovery.

By comparing the marginal increase in recovery ratio to the marginal increase in TMP, it was shown that raising TMP could lead to lower energy penalties per unit permeate recovered when operating at very low TMP's. The trends observed suggest the presence of an optimal operating point for the module.

Bibliography

[1] P. Eriksson, Nanofiltration extends the range of membrane filtration, Environmental Progress 7 (1) (1988) 58–62. doi:10.1002/ep.3300070116.

[2] A. Mohammad, Y. Teow, W. Ang, Y. Chung, D. Oatley-Radcliffe, N. Hilal, Nanofiltration membranes review: Recent advances and future prospects, Desalination 356 (2015) 226 – 254, State-of-the-Art Reviews in Desalination. doi:http://dx.doi.org/10.1016/j.desal.2014.10.043.

[3] H. Sombekke, D. Voorhoeve, P. Hiemstra, Environmental impact assessment of groundwater treatment with nanofiltration, Desalination 113 (2–3) (1997) 293 – 296, Workshop on Membranes in Drinking Water Production Technical Innovations and Health Aspects. doi:http://dx.doi.org/10.1016/S0011-9164(97)00144-6.

[4] R. A. Bergman, Membrane softening versus lime softening in Florida: A cost comparison update, Desalination 102 (1–3) (1995) 11 – 24, Proceedings of the American Desalting Association 1994 Biennial Conference and Exposition Membrane and Desalting Technologies. doi:http://dx.doi.org/10.1016/0011-9164(95)00036-2.

[5] M. Soltanieh, M. Mousavi, Application of charged membranes in water softening: modeling and experiments in the presence of polyelectrolytes, Journal of Membrane Science 154 (1) (1999) 53 – 60. doi:http://dx.doi.org/10.1016/S0376-7388(98)00285-3.

[6] M. Bodzek, S. Koter, K. Wesołowska, Application of membrane techniques in a water softening process, Desalination 145 (1–3) (2002) 321 – 327. doi:http://dx.doi.org/10.1016/S0011-9164(02)00430-7.

[7] S. Ghizellaoui, A. Chibani, S. Ghizellaoui, Use of nanofiltration for partial softening of very hard water, Desalination 179 (1–3) (2005) 315 – 322, membranes in Drinking and Industrial Water Production. doi:http://dx.doi.org/10.1016/j.desal.2004.11.077.

[8] C. M. Galanakis, G. Fountoulis, V. Gekas, Nanofiltration of brackish groundwater by using a polypiperazine membrane, Desalination 286 (2012) 277 – 284. doi:http://dx.doi.org/10.1016/j.desal.2011.11.035.

[9] F. Elazhar, R. Elhabbani, M. Elazhar, M. Hafsi, A. Elmidaoui, Comparison of the performances of two commercial membranes in hardness removal from underground water using nanofiltration membranes, International Journal of Advanced Chemistry 1 (2) (2013) 21–30.

[10] W. L. Ang, A. W. Mohammad, N. Hilal, C. P. Leo, A review on the applicability of integrated/hybrid membrane processes in water treatment and desalination plants, Desalination 363 (2015) 2 – 18, hybrid Systems for Desalination. doi:http://dx.doi.org/10.1016/j.desal.2014.03.008.

[11] M. Park, J. Park, E. Lee, J. Khim, J. Cho, Application of nanofiltration pretreatment to remove divalent ions for economical seawater reverse osmosis desalination, Desalination and Water Treatment (2015) 1–10arXiv:http://dx.doi.org/10.1080/19443994.2015.1111807, doi:10.1080/19443994.2015.1111807.

[12] C. Liu, L. Shi, R. Wang, Enhanced hollow fiber membrane performance via semi-dynamic layer-by-layer polyelectrolyte inner surface deposition for nanofiltration and forward osmosis applications, Reactive and Functional Polymers 86 (2015) 154 – 160. doi:http://dx.doi.org/10.1016/j.reactfunctpolym.2014.07.018.

[13] C. Liu, L. Shi, R. Wang, Crosslinked layer-by-layer polyelectrolyte nanofiltration hollow fiber membrane for low-pressure water softening with the presence of SO_4^{2-} in feed water, Journal of Membrane Science 486 (2015) 169 – 176. doi:http://dx.doi.org/10.1016/j.memsci.2015.03.050.

[14] H. I. Mahon, Permeability separatory apparatus, permeability separatory membrane element, method of making the same and process utilizing the same, U.S. Patent No. 3,228,876 (Jan. 11 1966).

[15] R. R. Donald, M. W. Everett, M. J. Murdock, Fluid separation process and apparatus, U.S. Patent No. 3,339,341 (Sep. 5 1967).

[16] N. Peng, N. Widjojo, P. Sukitpaneenit, M. M. Teoh, G. G. Lipscomb, T.-S. Chung, J.-Y. Lai, Evolution of polymeric hollow fibers as sustainable technologies: Past, present, and future, Progress in Polymer Science 37 (10) (2012) 1401 – 1424, topical Issue on Polymer Physics. doi:http://dx.doi.org/10.1016/j.progpolymsci.2012.01.001.

[17] R. W. Baker, Membrane Technology and Applications, John Wiley & Sons, Ltd, 2004. doi:10.1002/0470020393.

[18] C. Feng, K. Khulbe, T. Matsuura, A. Ismail, Recent progresses in polymeric hollow fiber membrane preparation, characterization and applications, Separation and Purification Technology 111 (2013) 43 – 71. doi:http://dx.doi.org/10.1016/j.seppur.2013.03.017.

[19] J. Hermans, Hydrodynamics of hollow fiber reverse osmosis modules, Membrane Digest 1.3 (1972).

[20] W. N. Gill, B. Bansal, Hollow fiber reverse osmosis systems analysis and design, AIChE Journal 19 (4) (1973) 823–831. doi:10.1002/aic.690190422.

[21] J. Happel, Viscous flow relative to arrays of cylinders, AIChE Journal 5 (2) (1959) 174–177. doi:10.1002/aic.690050211.

[22] B. Bansal, W. Gill, Theoretical experimental study of radial flow hollow fiber reverse osmosis, in: AIChE Symp. Ser., Vol. 70, 1974, pp. 136–149.

[23] M. S. Dandavati, M. R. Doshi, W. N. Gill, Hollow fiber reverse osmosis: experiments and analysis of radial flow systems, Chemical Engineering Science 30 (8) (1975) 877 – 886. doi:http://dx.doi.org/10.1016/0009-2509(75)80052-2.

[24] H. Ohya, H. Nakajima, K. Takagi, S. Kagawa, Y. Negishi, An analysis of reverse osmotic characteristics of B-9 hollow fiber module, Desalination 21 (3) (1977) 257 – 274. doi:http://dx.doi.org/10.1016/S0011-9164(00)88245-4.

[25] J. Hermans, Physical aspects governing the design of hollow fiber modules, Desalination 26 (1) (1978) 45 – 62. doi:http://dx.doi.org/10.1016/S0011-9164(00)84127-2.

[26] W. Bruining, A general description of flows and pressures in hollow fiber membrane modules, Chemical Engineering Science 44 (6) (1989) 1441 – 1447. doi:http://dx.doi.org/10.1016/0009-2509(89)85016-X.

[27] M. Sekino, Precise analytical model of hollow fiber reverse osmosis modules, Journal of Membrane Science 85 (3) (1993) 241 – 252. doi:http://dx.doi.org/10.1016/0376-7388(93)85278-5.

[28] M. Sekino, Study of an analytical model for hollow fiber reverse osmosis module systems, Desalination 100 (1–3) (1995) 85 – 97. doi:http://dx.doi.org/10.1016/0011-9164(96)00010-0.

[29] R. P. Ma, C. H. Gooding, W. K. Alexander, A dynamic model for low-pressure, hollow-fiber ultrafiltration, AIChE Journal 31 (10) (1985) 1728–1732. doi:10.1002/aic.690311018.

[30] N. C. Mat, Y. Lou, G. G. Lipscomb, Hollow fiber membrane modules, Current Opinion in Chemical Engineering 4 (2014) 18 – 24. doi:http://dx.doi.org/10.1016/j.coche.2014.01.002.

[31] J. K. Park, H. N. Chang, Flow distribution in the fiber lumen side of a hollow-fiber module, AIChE Journal 32 (12) (1986) 1937–1947. doi:10.1002/aic.690321202.

[32] S. Wickramasinghe, M. J. Semmens, E. Cussler, Mass transfer in various hollow fiber geometries, Journal of Membrane Science 69 (3) (1992) 235 – 250. doi:http://dx.doi.org/10.1016/0376-7388(92)80042-I.

[33] S. Elmore, G. G. Lipscomb, Analytical approximations of the effect of a fiber size distribution on the performance of hollow fiber membrane separation devices, Journal of Membrane Science 98 (1–2) (1995) 49 – 56. doi:http://dx.doi.org/10.1016/0376-7388(94)00174-W.

[34] V. Chen, M. Hlavacek, Application of Voronoi tessellation for modeling randomly packed hollow-fiber bundles, AIChE Journal 40 (4) (1994) 606–612. doi:10.1002/aic.690400405.

[35] L.-Z. Zhang, Heat and mass transfer in a randomly packed hollow fiber membrane module: A fractal model approach, International Journal of Heat and Mass Transfer 54 (13–14) (2011) 2921 – 2931. doi:http://dx.doi.org/10.1016/j.ijheatmasstransfer.2011.03.005.

[36] V. Silva, V. Geraldes, A. B. Alves, L. Palacio, P. Prádanos, A. Hernández, Multi-ionic nanofiltration of highly concentrated salt mixtures in the seawater range, Desalination 277 (1–3) (2011) 29 – 39. doi:http://dx.doi.org/10.1016/j.desal.2011.03.088.

[37] K. Wesolowska, S. Koter, M. Bodzek, Modelling of nanofiltration in softening water, Desalination 162 (2004) 137 – 151. doi:http://dx.doi.org/10.1016/S0011-9164(04)00037-2.

[38] B. Saliha, F. Patrick, S. Anthony, Investigating nanofiltration of multi-ionic solutions using the steric, electric and dielectric exclusion model, Chemical Engineering Science 64 (17) (2009) 3789 – 3798. doi:http://dx.doi.org/10.1016/j.ces.2009.05.020.

[39] W. Fang, L. Shi, R. Wang, Interfacially polymerized composite nanofiltration hollow fiber membranes for low-pressure water softening, Journal of Membrane Science 430 (2013) 129 – 139. doi:http://dx.doi.org/10.1016/j.memsci.2012.12.011.

[40] T. Tsuru, S.-i. Nakao, S. Kimura, Calculation of ion rejection by extended Nernst–Planck equation with charged reverse osmosis membranes for single and mixed electrolyte solutions, Journal of Chemical Engineering of Japan 24 (4) (1991) 511–517. doi:10.1252/jcej.24.511.

[41] X.-L. Wang, T. Tsuru, S. ichi Nakao, S. Kimura, Electrolyte transport through nanofiltration membranes by the space-charge model and the comparison with teorell-meyer-sievers model, Journal of Membrane Science 103 (1–2) (1995) 117 – 133. doi:http://dx.doi.org/10.1016/0376-7388(94)00317-R.

[42] W. Bowen, H. Mukhtar, Characterisation and prediction of separation performance of nanofiltration membranes, Journal of Membrane Science 112 (2) (1996) 263 – 274. doi:http://dx.doi.org/10.1016/0376-7388(95)00302-9.

[43] W. Bowen, A. Mohammad, N. Hilal, Characterisation of nanofiltration membranes for predictive purposes — use of salts, uncharged solutes and atomic force microscopy, Journal of Membrane Science 126 (1) (1997) 91 – 105. doi:http://dx.doi.org/10.1016/S0376-7388(96)00276-1.

[44] W. Bowen, A. Wahab Mohammad, Diafiltration by nanofiltration: Prediction and optimization, AIChE Journal 44 (8) (1998) 1799–1812. doi:10.1002/aic.690440811.

[45] J. Schaep, C. Vandecasteele, A. W. Mohammad, W. R. Bowen, Analysis of the salt retention of nanofiltration membranes using the donnan–steric partitioning pore model, Separation Science and Technology 34 (15) (1999) 3009–3030. arXiv:http://dx.doi.org/10.1081/SS-100100819, doi:10.1081/SS-100100819.

[46] W. Bowen, J. S. Welfoot, Modelling the performance of membrane nanofiltration—critical assessment and model development, Chemical Engineering Science 57 (7) (2002) 1121 – 1137. doi:http://dx.doi.org/10.1016/S0009-2509(01)00413-4.

[47] S. Bandini, D. Vezzani, Nanofiltration modeling: the role of dielectric exclusion in membrane characterization, Chemical Engineering Science 58 (15) (2003) 3303 – 3326. doi:http://dx.doi.org/10.1016/S0009-2509(03)00212-4.

[48] V. Geraldes, A. M. B. Alves, Computer program for simulation of mass transport in nanofiltration membranes, Journal of Membrane Science 321 (2) (2008) 172 – 182. doi:http://dx.doi.org/10.1016/j.memsci.2008.04.054.

[49] Y. Roy, M. H. Sharqawy, J. H. Lienhard V, Modeling of flat-sheet and spiral-wound nanofiltration configurations and its application in seawater nanofiltration, Journal of Membrane Science 493 (2015) 360 – 372. doi:http://dx.doi.org/10.1016/j.memsci.2015.06.030.

[50] W. M. Deen, Hindered transport of large molecules in liquid-filled pores, AIChE Journal 33 (9) (1987) 1409–1425. doi:10.1002/aic.690330902.

[51] P. Dechadilok, W. M. Deen, Hindrance factors for diffusion and convection in pores, Industrial & Engineering Chemistry Research 45 (21) (2006) 6953–6959. arXiv:http://dx.doi.org/10.1021/ie051387n, doi:10.1021/ie051387n.

[52] G. M. Mavrovouniotis, H. Brenner, Hindered sedimentation, diffusion, and dispersion coefficients for brownian spheres in circular cylindrical pores, Journal of Colloid and Interface Science 124 (1) (1988) 269 – 283. doi:http://dx.doi.org/10.1016/0021-9797(88)90348-7.

[53] J. Ennis, H. Zhang, G. Stevens, J. Perera, P. Scales, S. Carnie, Mobility of protein through a porous membrane, Journal of Membrane Science 119 (1) (1996) 47 – 58. doi:http://dx.doi.org/10.1016/0376-7388(96)00112-3.

[54] L. R. Glicksman, J. H. Lienhard V, Modeling and Approximation in Heat Transfer, Cambridge University Press, 2016.

[55] S. Sablani, M. Goosen, R. Al-Belushi, M. Wilf, Concentration polarization in ultrafiltration and reverse osmosis: a critical review, Desalination 141 (3) (2001) 269 – 289. doi:http://dx.doi.org/10.1016/S0011-9164(01)85005-0.

[56] V. Geraldes, M. D. Afonso, Prediction of the concentration polarization in the nanofiltration/reverse osmosis of dilute multi-ionic solutions, Journal of Membrane Science 300 (1–2) (2007) 20 – 27. doi:http://dx.doi.org/10.1016/j.memsci.2007.04.025.

[57] A. I. Schäfer, A. G. Fane, T. D. Waite, Nanofiltration: principles and applications, Elsevier, 2005.

[58] A. Grodzinsky, Field, Forces and Flows in Biological Systems, Garland Science, 2011.

[59] F. G. Donnan, Theory of membrane equilibria and membrane potentials in the presence of non-dialysing electrolytes. a contribution to physical-chemical physiology, Journal of Membrane Science 100 (1) (1995) 45–55.

[60] K. Dill, S. Bromberg, Molecular driving forces: statistical thermodynamics in biology, chemistry, physics, and nanoscience, Garland Science, 2010.

[61] D. L. Parkhurst, C. Appelo, User's guide to PHREEQC (Version 2): A computer program for speciation, batch-reaction, one-dimensional transport, and inverse geochemical calculations.

[62] K. H. Mistry, H. A. Hunter, J. H. Lienhard V, Effect of composition and nonideal solution behavior on desalination calculations for mixed electrolyte solutions with comparison to seawater, Desalination 318 (2013) 34 – 47. doi:http://dx.doi.org/10.1016/j.desal.2013.03.015.

[63] R. Silbey, R. Alberty, M. Bawendi, Physical Chemistry 4th edn, Wiley, New York, 2004.

[64] J. C. Giddings, E. Kucera, C. P. Russell, M. N. Myers, Statistical theory for the equilibrium distribution of rigid molecules in inert porous networks. exclusion chromatography, The Journal of Physical Chemistry 72 (13) (1968) 4397–4408. arXiv:http://dx.doi.org/10.1021/j100859a008, doi:10.1021/j100859a008.

[65] A. E. Yaroshchuk, Dielectric exclusion of ions from membranes, Advances in Colloid and Interface Science 85 (2–3) (2000) 193 – 230. doi:http://dx.doi.org/10.1016/S0001-8686(99)00021-4.

[66] M. H. Sharqawy, J. H. Lienhard V, S. M. Zubair, Thermophysical properties of seawater: a review of existing correlations and data, Desalination and Water Treatment 16 (1-3) (2010) 354–380. arXiv:http://dx.doi.org/10.5004/dwt.2010.1079, doi:10.5004/dwt.2010.1079.

[67] K. G. Nayar, M. H. Sharqawy, L. D. Banchik, J. H. Lienhard V, Thermophysical properties of seawater: A review and new correlations that include pressure dependence, Desalination 390 (2016) 1 – 24. doi:http://dx.doi.org/10.1016/j.desal.2016.02.024.

[68] W. Bowen, A. Mohammad, Characterization and prediction of nanofiltration membrane performance—a general assessment, Chemical Engineering Research and Design 76 (8) (1998) 885 – 893, separation Processes. doi:http://dx.doi.org/10.1205/026387698525685.

[69] G. H. McKinley, 2.25, Advanced Fluid Mechanics, Fall 2013. Massachusetts Institute of Technology: MIT OpenCourseWare, http://ocw.mit.edu, (Accessed 11 Apr 2016).
URL http://ocw.mit.edu

[70] F. M. White, Fluid Mechanics, Seventh Edition, McGraw-Hill Education, 2010.

[71] A. Bezdek, W. Kuperberg, Maximum density space packing with congruent circular cylinders of infinite length, Mathematika 37 (01) (1990) 74–80.

[72] F. Lipnizki, R. W. Field, Mass transfer performance for hollow fibre modules with shell-side axial feed flow: using an engineering approach to develop a framework, Journal of Membrane Science 193 (2) (2001) 195 – 208. doi:http://dx.doi.org/10.1016/S0376-7388(01)00512-9.

[73] J. H. Lienhard V, K. H. Mistry, M. H. Sharqawy, G. P. Thiel, Thermodynamics, Exergy, and Energy Efficiency in Desalination Systems, in: H. A. Arafat (Ed.), Desalination Sustainability: A Technical, Socioeconomic, and Environmental Approach, Chpt. 5, Elsevier Publishing Co., 2016 (in press).

[74] G. K. Pearce, UF/MF Membrane Water Treatment: Principles and Design, Water Treatment Academy Bangkok, 2011.

[75] DOW Chemical Company, Ultrafiltration Product Manual, 2011.

[76] Koch Membrane Systems, Puron MP Hollow Fiber Cartridge, 2015.

[77] N. S. Kotrappanavar, A. Hussain, M. Abashar, I. S. Al-Mutaz, T. M. Aminabhavi, M. N. Nadagouda, Prediction of physical properties of nanofiltration membranes for neutral and charged solutes, Desalination 280 (1–3) (2011) 174 – 182. doi:http://dx.doi.org/10.1016/j.desal.2011.07.007.

[78] R. Rautenbach, A. Gröschl, Separation potential of nanofiltration membranes, Desalination 77 (1990) 73–84.

[79] J. Garcia-Aleman, J. M. Dickson, Permeation of mixed-salt solutions with commercial and pore-filled nanofiltration membranes: membrane charge inversion phenomena, Journal of Membrane Science 239 (2) (2004) 163 – 172. doi:http://dx.doi.org/10.1016/j.memsci.2004.02.036.

[80] T. Tsuru, M. Urairi, S.-I. Nakao, S. Kimura, Negative rejection of anions in the loose reverse osmosis separation of mono-and divalent ion mixtures, Desalination 81 (1-3) (1991) 219–227.

[81] W. R. Bowen, J. S. Welfoot, P. M. Williams, Linearized transport model for nanofiltration: Development and assessment, AIChE Journal 48 (4) (2002) 760–773. doi:10.1002/aic.690480411.

[82] A. E. Yaroshchuk, Negative rejection of ions in pressure-driven membrane processes, Advances in Colloid and Interface Science 139 (1–2) (2008) 150 – 173, membrane Electrochemistry: Selected papers from the 33rd Conference on Membrane Electrochemistry, Russia, May 2007. doi:http://dx.doi.org/10.1016/j.cis.2008.01.004.

[83] A. M. Mika, R. F. Childs, J. M. Dickson, Ultra-low pressure water softening: a new approach to membrane construction, Desalination 121 (2) (1999) 149 – 158. doi:http://dx.doi.org/10.1016/S0011-9164(99)00016-8.

[84] M. Costello, A. Fane, P. Hogan, R. Schofield, The effect of shell side hydrodynamics on the performance of axial flow hollow fibre modules, Journal of Membrane Science 80 (1) (1993) 1 – 11. doi:http://dx.doi.org/10.1016/0376-7388(93)85127-I.